Decoding spine nanostructure in cultured neurons derived from mouse models of mental disorder reveals a schizophrenia-linked role for Ecrg4

Yutaro Kashiwagi[1], Qingrui Liu[1], Yasuhiro Go[2, 3,4], Ryo Saito[5], Atsu Aiba[5], Takanobu Nakazawa[6], and Shigeo Okabe[1,7,*]

[1]Department of Cellular Neurobiology, Graduate School of Medicine, the University of Tokyo, Tokyo 113-0033, Japan

[2]Graduate School of Information Science, University of Hyogo, Kobe 650-0047, Japan

[3]National Institute for Physiological Sciences (NIPS), National Institutes of Natural Sciences, Okazaki 444-8585, Japan

[4]Exploratory Research Center on Life and Living Systems (ExCELLS), National Institutes of Natural Sciences, Okazaki 444-8585, Japan

[5]Laboratory of Animal Resources, Center for Disease Biology and Integrated Medicine, Graduate School of Medicine, the University of Tokyo, Tokyo, 113-0033, Japan

[6]Department of Bioscience, Faculty of Life Sciences, Tokyo University of Agriculture, Tokyo 156-8502, Japan

[7] Laboratory for Imaging Neural Dynamics, RIKEN Center for Brain Science, Saitama 351-0198, Japan

[*]Corresponding author: Shigeo Okabe

Laboratory for Imaging Neural Dynamics, RIKEN Center for Brain Science, 2-1 Hirosawa, Wako, Saitama 351-0198, Japan

Phone: +81-(0)50-3500-7186

E-mail: shigeo.okabe@riken.jp

Abstract

Dendritic spine dysfunction may contribute to the etiology and symptom expression of neuropsychiatric disorders. The intimate relationship between spine morphology and function suggests that decoding disease-related abnormalities from spine morphology can aid in developing synapse-targeted interventions. Here, we describe a population analysis of dendritic spine nanostructure applied to the objective grouping of multiple mouse models of neuropsychiatric disorders. This method has identified two major groups of spine phenotypes linked to schizophrenia and autism spectrum disorder (ASD). An increase in spine subpopulation with small volumes characterized the spines of schizophrenia-associated mouse models, whereas a spine subset with large volumes increased in ASD models. Schizophrenia-associated mouse models showed higher similarity in spine morphology, driven by reduced size and growth of nascent spines. The expression of Ecrg4, a gene encoding small secretory peptides, was increased in schizophrenia-associated mouse models, and functional studies confirmed its critical involvement in impaired spine dynamics and shape. These results suggest that population-level spine analysis provides rich insights into heterogeneous spine pathology, facilitating the identification of new molecular targets related to core synaptic dysfunction.

Introduction

Information processing in the neocortex and hippocampus relies on fast excitatory synaptic transmission between pyramidal neurons. Many excitatory synapses that release glutamate project onto tiny structures protruding from dendritic shafts termed spines, and the morphological properties of these spines strongly influence synaptic transmission and function, including the activity-dependent synaptic plasticity implicated in learning and memory[1,2]. In general, larger spines contain a greater number of glutamate receptors and are functionally stronger[3]. The morphological parameters defining spine shape, such as length, radius, and volume, are also highly dynamic. For instance, small nascent spines can be enlarged by high-frequency stimuli, inducing long-term potentiation (LTP) of synaptic transmission[4,5]; alternatively, spine volume can be reduced by low-frequency stimuli that induce long-term depression (LTD)[5,6]. Due to these dynamic changes, spines on pyramidal neurons exhibit substantial morphological variation, even within the same dendritic branch. In addition to direct synaptic activation inducing LTP or LTD, spine morphology can be altered by cyclical hormonal changes, neuromodulators, and various activity-independent processes[7–10]. In turn, these changes in spine morphology are associated with marked changes in neural function and behavior.

Recent advances in super-resolution microscopy have provided new opportunities for the study of spine structural diversity and dynamics. An investigation using stimulated emission depletion (STED) imaging reported an increase in spine neck size after LTP, resulting in stronger electrical coupling between the spine head and the dendritic shaft[11]. A structured illumination microscopy (SIM) imaging study of

70 cultured hippocampal neurons revealed expansion of the spine head convexity after
71 LTP induction[12], and suggested that this structural transformation may increase the
72 adhesion of presynaptic and postsynaptic membranes. SIM imaging has also been
73 applied to record the dynamic properties of spinules[13], thin protrusions extending from
74 existing spines that may function in secondary synapse formation. Collectively, these
75 reports implicate spine nanostructural dynamics in multiple core synaptic properties
76 and functions, including neurotransmission, mechanical stability, synaptogenesis, and
77 plasticity.

78 Genetic mutations and variants that disrupt synaptic function are strongly
79 implicated in the pathogenesis of neuropsychiatric disorders such as autism spectrum
80 disorder (ASD) and schizophrenia[14–20]. Based on these genomic aberrations, numerous
81 mouse models of ASD and schizophrenia have been established and subsequently
82 shown to harbor abnormalities in both spine morphology and physiology[19,21–24].
83 Moreover, several studies have reported synaptic dysfunction in neurons differentiated
84 from patient-derived pluripotent stem cells [25–28]. Schizophrenia and ASD share several
85 clinical features, suggesting common genetic risk factors and etiology[29,30]. However, a
86 diametrical model emphasizes the distinct social-cognitive properties of these two
87 major psychiatric disorders[31,32]. Both ASD and schizophrenia also show highly
88 heterogeneous clinical phenotypes, potentially stemming from distinct pathogenic
89 processes within disease categories. Therefore, in addition to clinical features,
90 comparative biological phenotyping of multiple ASD and schizophrenia models may
91 reveal shared as well as disease-specific pathogenic processes.

92 Genetic studies on ASD and schizophrenia have identified copy-number

93 variants and protein-disrupting single-nucleotide variants that confer higher disease
94 risk, and mouse models harboring these genetic abnormalities frequently exhibit
95 behavioral and neurological features resembling those of the clinical conditions (termed
96 endophenotypes)[19,33]. However, only a limited number of studies objectively compare
97 phenotypes related to synaptic structure and function across disease models. An *in*
98 *vivo* two-photon imaging study reported accelerated spine turnover in three genetically
99 distinct mouse models of ASD[34]. Also, multiple mouse models of ASD were found to
100 exhibit a similar imbalance in the activity of excitatory and inhibitory neurons[35]. These
101 studies support the idea that distinct genetic mutations may induce similar synaptic and
102 circuit phenotypes in ASD-associated mouse models. However, differences in synaptic
103 properties between ASD and schizophrenia have not yet been comprehensively
104 examined.

105 In this study, we developed an objective method for identifying population-
106 level differences in spine nanostructure. This method, which has been applied to
107 multiple mouse models of psychiatric disorders, identified two distinct groups
108 corresponding to ASD and schizophrenia. An increase in a specific spine
109 subpopulation with small volumes characterized the spines of mouse models of
110 schizophrenia. In turn, ASD-related mouse models showed an opposite spine
111 phenotype. The schizophrenia-related phenotype was associated with reduced size
112 and growth of nascent spines and enhanced spine turnover. Further gene expression
113 analysis identified the overexpression of Ecrg4, a gene encoding a precursor of
114 hormone-like peptides, as a candidate mediator of this schizophrenia-associated spine
115 phenotype. Population-level analysis of spine nanostructures is a powerful approach
116 for understanding heterogeneous synaptic impairments in psychiatric disorders.

Results

Spine nanostructure imaging and generation of the spine density plot

We have designed a method for objectively comparing spine properties among multiple mouse models of psychiatric disorders at the population level using SIM imaging. Previous results demonstrated that high-resolution SIM images of dendritic spines in cultured hippocampal neurons can provide reliable information about spine size and morphological properties[12]. In the current study, the analytical procedures for SIM images were further improved for quantitative comparisons. Three-dimensional SIM images of dendritic spines were captured in DiI-stained cultured neurons derived from control and disease-model mouse hippocampus (Figure 1A). This staining procedure provided a better image quality than fluorescent protein-based labeling because of the higher fluorescence signal from the plasma membrane. SIM images were processed using custom-made scripts to identify and segment the individual dendritic spines (Figure 1B–D). We previously reported a set of scripts designed to isolate dendritic spines automatically[12]. However, the segmentation accuracy still necessitated manual inspection. In the newly developed scripts, we introduced a step to readjust the spine–shaft boundary, enabling fully automated measurement of multiple morphological parameters, including length, surface area, and volume. In addition, the isolated spines were further divided into 160-nm-thick longitudinal segments, yielding a total of 64 shape descriptors.

Spine shape parameters measured by conventional methods are difficult to compare directly when images are obtained from multiple independent experiments.

140 This problem is caused by several factors, but the main factors are variability in image
141 intensity, signal-to-noise ratio, and image aberration introduced by unoptimized
142 imaging conditions. To test the stability of SIM-based spine imaging, we compared the
143 spine size distribution across four samples prepared at time points separated by >2
144 months (Supplementary Figure 1). The cumulative distribution curves of the four
145 datasets showed extensive overlap, confirming the reproducibility of the SIM-based
146 spine shape measurements using independent culture samples.

147 Another technical issue in comparing spine shape is the heterogeneity of
148 spine shapes and the absence of defined subclasses. Population-level spine analysis,
149 therefore, requires a new strategy that enables objective comparisons of large numbers
150 of spines with a continuum of morphologic features. We previously demonstrated that
151 principal component analysis (PCA) was effective for comparing high-dimensional
152 spine shape features (descriptors) in a reduced-dimensional feature space[12]. Indeed, a
153 PCA-based dimensional reduction of a large number of spines, based on their
154 descriptors, generated a two-dimensional plot of spine shape that closely matched
155 conventional spine subtypes, such as thin, mushroom, and stubby (Figure 1E). To
156 objectively compare the two spine datasets (control and disease model), we first
157 generated plots of relative spine densities (number per area in feature space) mapped
158 to 80 × 80 square blocks (Figure 1F), and then subtracted the corresponding plot pairs
159 defined by genotype (control vs. mutant) or culture conditions. The resulting subtracted
160 density plots contain comprehensive information about the differences in relative spine
161 numbers with similar shape properties. As expected, there was some variation in the
162 density plot patterns across experiments. However, subtracting the distributional data
163 from wild-type and mutant samples effectively canceled out these differences.

164 Moreover, the difference between the two wild-type samples was generally smaller
165 than that between wild-type and mutant samples.

166

167 **Comparison and grouping of multiple mouse models based on morphological**
168 **spine similarity**

169 The subtracted density plots contain rich information about the population-level
170 differences in spine shape between samples. Therefore, the generation and
171 comparison of the plots for both ASD- and schizophrenia-associated mouse models will
172 be useful for their unbiased grouping. We selected the following eight representative
173 mouse models harboring either copy-number variation or single gene mutations
174 associated with psychiatric disorders: male hemizygous or female homozygous mutant
175 mice for neuroligin-3 R451C mutation (Nlgn3$^{R451C/(y\ or\ R451C)}$)[36,37], heterozygous Syngap1
176 mutant mice (Syngap1$^{+/-}$)[38], heterozygous POGZ mutant mice (POGZ$^{Q1038R/+}$)[39], mice
177 paternal duplication of chromosome 7C (15q11-13$^{dup/+}$) corresponding to human 15q11-
178 13 duplication[40], mice with heterozygous deletion of chromosome 16B2,3 (3q29$^{del/+}$)
179 corresponding to human 3q29 deletion[41], mice heterozygous for deletion on
180 chromosome 16qA13 (22q11.2$^{del/+}$) corresponding to 1.5 Mb deletion on human
181 22q11.2[42], mice heterozygous for Setd1a mutation (Setd1a$^{+/-}$)[43], and Ca^{2+}/calmodulin-
182 dependent protein kinase IIα kinase-dead mutant mice (CaMKIIα$^{K42R/K42R}$)[44]. Previous
183 studies on these mouse models confirmed the presence of multiple sensory, memory,
184 and social endophenotypes of psychiatric disorders compared to controls. Of these,
185 Nlgn3$^{R451C/(y\ or\ R451C)}$, POGZ$^{Q1038R/+}$, and 15q11-13$^{dup/+}$ models mimic genetic variations
186 found in ASD. Human mutations in the SYNGAP1 gene are associated with intellectual

187 disability and autistic behaviors. The 3q29$^{del/+}$, 22q11.2$^{del/+}$, and Setd1a$^{+/-}$ models harbor
188 genetic mutations associated with higher schizophrenia risk. CaMKII-related signaling
189 pathway disruption has been implicated in the working memory deficits found in
190 schizophrenia patients[45,46]. CAMK2A mutations in humans are linked to multiple mental
191 disorders, including developmental disorders, ASD, and schizophrenia[47]. The K42R
192 mutation of CAMK2A does not correspond to any known human genetic variant, but the
193 CAMK2A R8H mutation is linked to schizophrenia[48]. Both R8H and K42R mutations in
194 the N-terminal domain of CaMKIIα eliminate kinase activity; these mutations may have
195 a similar impact on human mental disorders. Taken together, these mouse models
196 cover a broad spectrum of human genetic aberrations associated with psychiatric
197 disorders. Direct comparison of spine phenotypes could therefore provide important
198 clues to underlying shared and disease-specific synaptic pathologies.

199 For these comparisons, we prepared three independent cultures of embryonic
200 hippocampi from each control–mutant pair and obtained 700–1,500 3D-SIM spine
201 images 3 weeks after plating for both mutant and control samples (Nlgn3$^{R451C/(y\ or\ R451C)}$,
202 n = 1,134 and 1,204; Syngap1$^{+/-}$, n = 991 and 1,371; POGZ$^{Q1038R/+}$, n = 1,341 and
203 1,271; 15q11-13$^{dup/+}$, n = 1,208 and 1,099; 3q29$^{del/+}$, n = 1,429 and 1,408; 22q11.2$^{del/+}$,
204 n = 1,143 and 914; Setd1a$^{+/-}$, n = 1,381 and 1,405; CaMKIIα$^{K42R/K42R}$; n = 880 and 763,
205 control and mutant, respectively, Supplementary Table 1). Initial comparison of the
206 cumulative frequency plots for spine length, spine surface area, and spine volume
207 alone did not provide sufficient information to infer their structural similarity
208 (Supplementary Figure 2), indicating that simple structural parameters are not effective
209 in identifying disease-specific spine shape characteristics. We next generated
210 subtracted density plots from 8 mouse models. These plots were variable, but there

211 were certain similarities between the specific mutants (Figure 2A). We evaluated
212 pairwise similarities by calculating the 2D cross-correlations of the subtracted density
213 plots. The matrix of these 2D cross-correlation values yielded two major groups with
214 high within-group similarity (Figure 2B), and this grouping was further confirmed by
215 unbiased clustering analysis (Figure 2C). The ASD models Nlgn3$^{R451C/(y\ or\ R451C)}$,
216 Syngap1$^{+/-,}$ and POGZ$^{Q1038R/+}$ were in the first group, while the second group contained
217 the schizophrenia models 3q29$^{del/+}$, 22q11.2$^{del/+}$, and Setd1a$^{+/-}$. This result is striking, as
218 it indicates that information about spine shape alone can distinguish whether the
219 culture preparation is derived from ASD- or schizophrenia-associated mouse models. It
220 is also of note that there were greater similarities among the schizophrenia-associated
221 mouse models than among the ASD-associated mouse models. This finding suggests
222 convergence in spine pathophysiology across schizophrenia-associated mouse
223 models.

224 In addition to the eight mouse models of psychiatric disorders, we generated
225 subtracted density plots for three additional conditions: immature culture samples (13
226 days in vitro, DIV), treatment with the AMPA subtype glutamate receptor blocker
227 CNQX, and treatment with the $GABA_A$ receptor blocker bicuculline (Figure 2A). The
228 subtracted density plots from the 13 DIV culture and the CNQX treatment were similar
229 to those of schizophrenia-associated mouse models. This finding suggests that the
230 hippocampal synapses in mouse models of schizophrenia are immature and inactive.
231 In contrast, the subtracted density plot of the bicuculline-treated sample was distinct
232 from that of both the schizophrenia and ASD-associated mouse models.

233

234 **Distinct spine shapes between ASD- and schizophrenia-associated mouse**
235 **models**

236 The subtracted density plots provide information on the structural properties of specific
237 spine subsets that either increased or decreased in disease mouse models. We first
238 defined the four areas within the PC1-PC2 plane with distinct shapes: (1) small and
239 short, (2) small and long, (3) large and short, and (4) large and long (Figure 3A and B).
240 We also identified the wildtype-enriched area (blue areas in Figure 3C and D) and the
241 mutant-enriched area (yellow areas in Figure 3C and D) in the same projection plane.
242 The comparison of these two types of areas suggests that larger spines are enriched in
243 the Nlgn3$^{R451C/(y\ or\ R451C)}$ mouse model, while small spines are enriched in the
244 22q11.2$^{del/+}$ mouse model. Next, we calculated the normalized spine counts in the four
245 areas for both wild-type and mutant samples and obtained the relative abundance
246 (mutant/wild-type) for each area (Figure 3E and F). The average of three independent
247 culture preparations confirmed the opposite trend between Nlgn3$^{R451C/(y\ or\ R451C)}$ and
248 22q11.2$^{del/+}$.

249 Figure 3G-J summarizes the relative abundance of mutant spines in four areas
250 with distinct spine shapes. We found that the relative abundance of mutant spines in
251 area 2 (small and long spines) differed significantly between genotypes (ANOVA, $p <$
252 0.001). Group comparisons by Tukey's post hoc test indicate significant differences
253 between Nlgn3$^{R451C/(y\ or\ R451C)}$ mutant and three schizophrenia-related mutants; 3q29$^{del/+}$,
254 22q11.2$^{del/+}$, and Setd1a$^{+/-}$ (Figure 3G). The opposite trend between areas 2 (small and
255 long spines) and 3 (large and short spines) further confirms distinct spine-shape
256 properties in ASD- and schizophrenia-related mouse models. The areas within the

257 subtracted density plots with enriched control or mutant spines illustrate the
258 characteristics of spine populations across mouse models (Supplementary Figures 3
259 and 4). The shape profiles of spines confirmed smaller spine volume of schizophrenia-
260 related mouse models (Supplementary Figure 5).

261

262 **Altered initial growth of dendritic spines in mouse models of schizophrenia**

263 The subtracted density plots reveal common changes in the spine population across
264 schizophrenia-associated mouse models. The mutant-spine-enriched areas also
265 contain small, elongated spines, suggesting dysfunction in either the generation of
266 nascent spines or the shrinkage of existing spines. To examine potential abnormalities
267 in spine dynamics, we performed time-lapse imaging of hippocampal neuron cultures
268 derived from two schizophrenia-associated mouse models, 22q11.2$^{del/+}$ and Setd1a$^{+/-}$,
269 and the Nlgn3$^{R451C/(y\ or\ R451C)}$ mouse model as a reference (Figure 4).

270 A linear mixed-effects model indicated significant effects of genotype in spine
271 turnover rate in both 22q11.2$^{del/+}$ and Setd1a$^{+/-}$ models ($F(1,25) = 5.79$, $p = 0.024$ for
272 22q11.2$^{del/+}$ and $F(1,22) = 7.33$, $p = 0.013$ for Setd1a$^{+/-}$). In contrast, no significant
273 effects were observed in the Nlgn3$^{R451C/(y\ or\ R451C)}$ model (Figure 5A-C). There was a
274 significant effect of genotype in both 22q11.2$^{del/+}$ and Setd1a$^{+/-}$ models also for the
275 prolonged lifetime of transient spines (a linear mixed-effects model: 22q11.2$^{del/+}$;
276 $F(1,336)=5.33$, $p=0.022$, Setd1a$^{+/-}$; $F(1,282)=6.38$, $p=0.012$), with no significant
277 difference in Nlgn3$^{R451C/(y\ or\ R451C)}$ model (Figure 5D-F).

278 We further compared the initial increase in spine volume between genotypes

279 (Figure 5G-I). Linear mixed-effects models incorporating nested random effects
280 revealed significantly smaller initial spine volumes in both 22q11.2$^{del/+}$ and Setd1a$^{+/-}$
281 models (genotype effect: $p < 0.001$ for 22q11.2$^{del/+}$ and $p < 10^{-7}$ for Setd1a$^{+/-}$). The
282 spines in both mutants also displayed a significant reduction in spine volume increase
283 ($p < 0.001$). In contrast, newly formed spines in the Nlgn3$^{R451C/(y\ or\ R451C)}$ neurons were
284 significantly larger than those in wild-type neurons ($p < 10^{-4}$) with preserved time-
285 course of spine growth.

286 Similar analyses of spine volume reduction before spine loss using linear
287 mixed-effects models identified significantly smaller initial spine size in the 22q11.2$^{del/+}$
288 model ($p < 10^{-6}$), while no significant differences in the initial spine volume were found
289 for the Setd1a$^{+/-}$ model (Figure 5J-L). The temporal trajectories of spine shrinkage
290 before their loss were not significantly altered in both 22q11.2$^{del/+}$ and Setd1a$^{+/-}$ models.
291 The Nlgn3$^{R451C/(y\ or\ R451C)}$ model showed a significantly different time-course of spine
292 shrinkage ($p < 0.05$), while the initial spine size was not altered. Taken together, these
293 results suggest that the smaller size of the initial spine, slower growth of nascent
294 spines, and enhanced spine turnover contribute to the development of schizophrenia-
295 related spine phenotypes.

296 To further examine the relationship between the spine growth rate and
297 lifetime, we performed simulations using the computational model shown in Figure 6A.
298 In this model, new spines appear randomly along the dendritic shaft according to a
299 density-dependent probability function, then increase in volume with speed V1 (phase
300 1), are eliminated with probability P1 (phase 2), and are converted to stable spines
301 upon reaching a volume threshold (phase 3). These stable spines are subsequently

302 destabilized with low probability P2 (phase 4) and start to shrink with speed V2 (phase
303 5). When these shrinking spines reach a threshold, they are permanently removed. We
304 did not incorporate the initial spine size as a model parameter because of its large
305 variability, which made parameter optimization difficult. This model was run over 10
306 days of neuronal differentiation in culture (corresponding to the period of spine density
307 increase from 8 to 17 DIV) with 625 different combinations of V1, V2, P1, and P2 to
308 identify the combination with the best fit to the experimental data for spine turnover of
309 15–18 DIV neurons derived from mutants 22q11.2$^{del/+}$, Setd1a$^{+/-}$, and Nlgn3$^{R451C/(y\ or}$
310 $^{R451C)}$ over 24 h (Figure 6B and Supplementary Figure 6A). The best-fitted models all
311 yielded spine lifespan distributions matching observations of the three mouse mutants
312 (Figure 6C). The two characteristics of the spines in 22q11.2$^{del/+}$ and Setd1a$^{+/-}$ were
313 also preserved in the best-fitted model. First, spine density in the schizophrenia-
314 associated mouse models was lower in both the simulation and experimental data
315 (simulation: 0.57 $\pm$ 0.029 /μm and 0.40 $\pm$ 0.027 /μm for the control and the best-fitted
316 for schizophrenia models, shown in Supplementary Figure 6B, experiment; 0.69 $\pm$ 0.17
317 /μm and 0.56 $\pm$ 0.20 /μm for the control and 22q11.2$^{del/+}$, 0.70 $\pm$ 0.15 /μm and 0.64 $\pm$
318 0.16 /μm for the control and Setd1a$^{+/-}$). Second, the size of transient spines was
319 smaller in schizophrenia-associated mouse models in the simulation (0.33 ± 0.033 and
320 0.20 ± 0.024 (a.u.) for the control and the best-fitted schizophrenia, Supplementary
321 Figure 6C), consistent with data on spine nanostructure (Figure 3G and J).

322 After the selection of the best-fitted parameters for three mouse models, we
323 compared the optimal values of V1, V2, P1, and P2 between mouse models (Figure
324 6D). The nascent spine volume increase (V1) was slower in schizophrenia models than
325 in corresponding controls. In turn, the probability of nascent spine loss (P1) was higher

326 in the ASD model. In all three disease models, the probability of spine destabilization
327 (P2) was moderately higher than that in the corresponding controls. Additional
328 simulation results with different P2 values indicate that P2 has a small effect on the
329 overall pattern of spine dynamics. These results suggest that a slow spine volume
330 increase in schizophrenia model mice results in the accumulation of nascent spines
331 with smaller volumes. On the other hand, the spines of ASD model mice grow at a rate
332 similar to that of control spines, but are more likely to be eliminated both in the nascent
333 stage and after maturation.

334 Simulated trajectory plots of individual spines along the dendritic shaft, using
335 the best-fit parameters, also reflected the differential patterns of spine turnover in
336 culture preparations derived from control and schizophrenia model mice (Figure 6E). In
337 culture preparations derived from schizophrenia-associated mouse models, there were
338 fewer spines with a lifetime longer than 2 or 3 days, while there was a greater number
339 of spines formed and eliminated within 24 h. This increase in the number of less stable
340 spines explains the pattern of spine lifetimes shown in Figure 5D-E. In summary, these
341 simulations suggest that a reduced spine maturation rate can account for three key
342 properties of schizophrenia-related spines: the greater number of small-volume spines,
343 enhanced turnover, and reduced spine density.

344

345 **Screening of molecules responsible for altered spine properties in**
346 **schizophrenia-associated mouse models**

347 Both SIM-based imaging and time-lapse imaging suggest that the initial growth phase
348 of spines is slower in schizophrenia model mice. To identify candidate genes that may

349 contribute to this growth impairment, we performed RNA sequencing of libraries
350 derived from the cultured neurons of eight psychiatric disorder mouse models and
351 corresponding controls, and filtered the results for differentially expressed genes
352 (DEGs) (Supplementary Table 2 and 3). The DEGs specific to more than two
353 schizophrenia-related mouse models are listed in Supplementary Figure 7. In the
354 hippocampi of schizophrenia model mice, the expression levels of Met, Osr1,
355 Arhgap15, and Rnf170-ps were downregulated, whereas those of Cip4, Ecrg4, and
356 Npas4 were upregulated. The majority of these DEGs have been previously implicated
357 in the pathology of schizophrenia (Met)[49], synaptic plasticity (Npas4)[50,51], or signaling
358 pathways in the nervous system (Arhgap15[52], Cip4[53], and Ecrg4[54]).

359 If these genes do regulate spines in schizophrenia-associated mouse models,
360 manipulation of these genes in wild-type neurons may induce a spine phenotype
361 similar to that observed in these models. To test this possibility, we downregulated Met
362 and Arhgap15, and upregulated Cip4, Ecrg4, and Npas4 in separate wild-type
363 hippocampal neuron cultures and measured spine dynamics using time-lapse imaging
364 (Figure 7A and B, Supplementary Figure 8). The application of a linear mixed-effects
365 model to knockdown experiments revealed no significant effect of treatment ($F(2,6) =$
366 0.29, $p = 0.76$). In the overexpression experiment, the analysis using a linear mixed-
367 effects model showed a significant main effect of treatment ($F(3,8) = 4.59$, $p = 0.038$),
368 with a significant increase in spine turnover rate by Ecrg4 overexpression ($\beta = 0.49 \pm$
369 0.16 SE, $t(8) = 3.16$, $p = 0.013$). Thus, the aberrant expression of Ecrg4 may be related
370 to the spine phenotype of schizophrenia model mice.

371 Ecrg4 encodes a precursor protein that yields several short hormone-like

372 peptides via multiple cleavage sites[55]. Ecrg4 has been reported to function in cell
373 proliferation, inflammation, and tumor suppression. However, there is limited
374 information on the neuronal functions of Ecrg4. Therefore, we further analyzed the
375 cellular distribution of Ecrg4 in wild-type hippocampal neurons to assess its potential
376 synaptic functions. The Ecrg4 protein was detected in the membrane fraction of
377 cultured hippocampal neurons (Supplementary Figure 9A). In addition, HA-tagged
378 Ecrg4 showed punctate localization patterns within the neuronal cytoplasm (Figure 7C).
379 A fraction of HA-tagged Ecrg4 puncta localized at axonal varicosities (arrowheads) or
380 dendritic spines (arrows), together with some extracellular clusters (asterisks). HA-
381 tagged Ecrg4 also colocalized with GFP-tagged neuropeptide Y (NPY) (Supplementary
382 Figure 9B and C), suggesting transport in dense-core vesicles. Surface labeling of live
383 cells also revealed clusters of Ecrg4 on axonal boutons and dendritic spines
384 (Supplementary Figure 9D and E), supporting active exocytosis and tethering via its
385 binding partners to the plasma membrane. Exogenous application of the synthetic
386 Ecrg4 peptide enhanced spine turnover (Supplementary Figure 9F and G). Collectively,
387 these observations suggest that the intracellular machinery for transporting and
388 releasing Ecrg4 may be actively involved in regulating synapse formation and
389 maturation.

390

391 **Rescue of the synaptic phenotype in schizophrenia-associated mouse models by**
392 **Ecrg4 suppression**

393 The spatial localization of Ecrg4 protein in wild-type neurons and upregulated gene
394 expression in the hippocampus of schizophrenia model mice strongly suggest a

395 contribution to the observed spine abnormalities. To examine this possibility, we tested
396 whether Ecrg4 suppression by Ecrg4-shRNA rescues the synaptic phenotype of
397 neurons derived from schizophrenia-associated mouse models (Supplementary Figure
398 8H and I). We introduced a GFP expression plasmid along with the Ecrg4-shRNA
399 plasmid or the control shRNA plasmid into neurons derived from 22q11.2$^{del/+}$ and
400 Setd1a$^{+/-}$ mice (Supplementary Table 1). The spine density plots generated from GFP-
401 expressing neurons differed from those generated from DiI-labeled neurons. This
402 difference may be due to the properties of SIM images obtained from either cell-surface
403 DiI labeling or cytoplasmic GFP expression. Nevertheless, the subtracted (differential)
404 distribution patterns between mutant and wild-type spines under the control shRNA
405 condition indicate the enrichment of small spines (Figure 8A and J). From these plots,
406 we identified the area showing enrichment of mutant spines (Figure 8B and K) and that
407 of wild-type spines (Figure 8C and L). The pattern of small spine enrichment in mutant
408 neurons shown in Figure 8A and J was no longer present in the plots generated by the
409 subtraction of the wild-type spines under control shRNA from the mutant spines under
410 Ecrg4 shRNA, indicating the possible rescue of the phenotype (Figure 8D and M).
411 Consistent with this interpretation, enrichment in both the mutant- and wild-type–
412 dominant regions was attenuated (Figure 8E, F, N, and O).

413 To determine whether the effect of Ecrg4 shRNA exceeded that expected from
414 random variation in spine counts, we performed a permutation analysis. Spine
415 identities were randomly reassigned between the two conditions while preserving the
416 total number of spines in each dataset, and the differential density maps were
417 recalculated for each permutation. This procedure generated a null distribution of
418 enrichment values expected under random assignment (Figure 8H, I, Q, and R). The

419 level of attenuation observed in both 22q11.2$^{del/+}$ and Setd1a$^{+/-}$ neurons exceeded the
420 95th percentile of the permuted distributions ($p < 0.05$), indicating that the obtained
421 data were unlikely to be explained by stochastic variation alone (Figure 8G and P). This
422 analysis supports the idea that Ecrg4 downregulation can rescue the spine-shape
423 impairment observed in schizophrenia-related mouse models.
424

Discussion

We developed an objective method for identifying population-level differences in spine nanostructures and applied it to cultured hippocampal neurons derived from multiple mouse models of psychiatric disorders. We identified two distinct groups of mouse models based on population-level spine properties. Notably, these two objectively identified groups correspond to mouse models with ASD-related gene mutations and schizophrenia-related gene mutations. A higher fraction of the small spine population was a common characteristic of schizophrenia-associated mouse models. Time-lapse imaging of spine dynamics revealed that this smaller spine phenotype is associated with a reduced initial size and growth of spines and their enhanced turnover. Screening for genes differentially expressed between mutant and control mice identified Ecrg4 overexpression as a potential molecular mechanism contributing to the schizophrenia spine phenotype. Indeed, suppression of Ecrg4 expression normalized the spine phenotype in neurons derived from schizophrenia-associated mouse models. These findings support the use of population-level analysis of spine nanostructures as a powerful approach to elucidating the heterogeneous synaptic impairments underlying psychiatric disorders.

Spine nanostructures provide information about developmental history, prior activity, and current functional properties, but these fine structural details were not accessible by conventional light microscopy. However, recent advances in super-resolution microscopy allow for the study of nanoscale spine morphology, including in living preparations, and have revealed new structural features related to important synaptic functions[11–13]. Another challenge to spine nanoscale imaging is the structural

448 heterogeneity across large spine populations, which may obscure important population-
449 level differences. Nonetheless, to understand the physiology and pathology of neural
450 networks, it is essential to obtain comprehensive information about a large number of
451 spines within a single neuron and across local neuronal networks. We previously
452 reported a dimensional reduction technique coupled with machine learning for
453 evaluating spine properties at the population level [12], and have further refined this
454 method for the current investigation to extract population-level nanostructural features
455 of spines in multiple mouse models of psychiatric disorders. This method enabled us to
456 compare spine phenotypes across different mouse models objectively and group
457 disease models based on similarities and differences in the spine population. Notably,
458 the two identified groups corresponded to ASD- and schizophrenia-related gene
459 mutations, supporting the idea that population-level analyses of spine nanostructures
460 provide meaningful information on synaptic abnormalities and dysfunction.

461 Population-level spine properties were more homogeneous in schizophrenia
462 models (those with gene mutations implicated in schizophrenia) than in the other 4
463 models studied, in part due to a shared tendency for smaller spines. This observation
464 is consistent with previous studies on Setd1a mutant mice, which showed reduced
465 spine width, decreased mushroom-type spines, and lower spine density in the
466 prefrontal cortex[43,56,57]. In contrast to these findings, several previous studies reported
467 reduced numbers of small spines in the postmortem cortical tissues of schizophrenia
468 patients[22,58]. However, this discrepancy may be attributed to the developmental period,
469 as we examined fetal neuronal spines after 3 weeks of in vitro differentiation, whereas
470 the aforementioned studies included postmortem samples from patients over 40 years
471 of age. One possible scenario that may help unify these observations is that spine

472 density is reduced in the early postnatal period, and that this reduction triggers
473 homeostatic plasticity, which, in turn, reduces the fraction of small spines in later life.
474 Another potential explanation is that schizophrenia differentially affects regional spine
475 properties (e.g., hippocampus versus cortex). Previous *in vivo* two-photon imaging
476 studies reported higher spine turnover in the hippocampus than the cortex[59,60].
477 Therefore, the spine phenotype identified in this study may be specific to hippocampal
478 pyramidal neurons. Finally, while the spine phenotype identified in the human
479 postmortem brain undoubtedly resulted from complex interactions among genetic
480 background, environmental influences, and regulation by non-neuronal cells, data from
481 pure neuronal cultures are more likely to reflect the direct effects of schizophrenia-
482 related gene mutations on synaptic functions. This property may be advantageous for
483 identifying synaptic molecules that regulate synapse phenotypes in schizophrenia-
484 related mouse models. However, the phenotype observed in the culture system
485 requires confirmation using in vivo experiments of mouse models or human tissue
486 samples. Efficient in vitro screening combined with reliable in vivo evaluation of
487 synapses will facilitate translational research on mental disorders.

488 In addition to Ecrg4, these analyses identified several other DEGs common to
489 mice harboring schizophrenia-related mutations. However, time-lapse imaging
490 identified Ecrg4 as the most effective spine regulator, and we also found that Ecrg4
491 suppression reversed the abnormal spine phenotype in neurons derived from
492 schizophrenia model mice. Ecrg4 encodes a precursor protein of hormone-like
493 peptides [61]. Exogenously expressed Ecrg4 exhibited a punctate pattern in both axonal
494 and dendritic compartments, with a fraction of clusters present on the cell surface. This
495 observation indicates that Ecrg4 may be secreted locally by axons or dendrites,

496 thereby influencing synapses and adjacent neurons. Several signaling pathways act
497 downstream of Ecrg4, including the stress-related NF-κB pathway and PI3K/Akt/mTOR
498 pathway[55]. Ecrg4-derived peptides may also act through Toll-like receptor 4 (TLR4) or
499 multiple scavenger receptors, such as LOX1[61]. While Ecrg4-related signaling pathways
500 have been studied primarily in the context of inflammation and infection, there are few
501 studies on Ecrg4-related signaling pathways in neurons. However, an Ecrg4-deficient
502 mouse model demonstrated enhancements in neural stem cell proliferation and spatial
503 learning, suggesting that overexpression may disrupt hippocampal function[54]. We
504 suggest that Ecrg4 may be a critical regulator of neural development and
505 synaptogenesis in the hippocampus. Further studies are warranted to identify Ecrg4
506 receptors and downstream signaling pathways and to investigate the potential
507 dysfunction of these pathways in schizophrenia-associated mouse models.

508 The nanoscale features of dendritic spines in ASD-associated mouse models
509 were more variable than those in schizophrenia-associated mouse models. This
510 difference may be related to the broader clinical spectrum of ASD, which ranges from
511 mild impairments in social skills to severe intellectual disability. The four ASD-
512 associated mouse models examined in this study, Nlgn3$^{R451C/(y\ or\ R451C)}$, Syngap1$^{+/-}$,
513 POGZ$^{Q1038R/+}$, and 15q11-13$^{dup/+}$, may represent subgroups with different levels of
514 hippocampal dysfunction. Among the four ASD-associated mouse models, 15q11-
515 13$^{dup/+}$ showed population-level spine properties closer to those of the schizophrenia
516 models. To understand this similarity, further analysis of neural circuit changes in both
517 ASD- and schizophrenia-associated mouse models will be necessary. Analysis of the
518 relationships between rare genetic variants and synapse phenotypes in mouse models
519 may contribute to their eventual categorization. This information should be useful to

520 understand the underlying mechanisms of the broader clinical spectrum of ASD.

521 The most important advantage of our analytical method is reproducibility,
522 despite the substantial heterogeneity in genotype and phenotype among these mouse
523 models. Thus, we are confident that the spine population analysis described here will
524 help researchers in different laboratories obtain reliable and comprehensive information
525 on spine properties. Further, this method could facilitate comparisons across a large
526 number of mouse models harboring mutations associated with mental disorders. Spine
527 morphology as measured in a reduced culture system can also demonstrate direct
528 effects of gene mutations on neuronal phenotypes in the absence of indirect influences
529 from nonneuronal cells or specific environments. Ultimately, these studies may identify
530 the shared and specific pathogenic mechanisms of psychiatric disorders and lead to
531 improved diagnosis and treatments.

532

533

534 **Materials and Methods**

535 **Neuronal culture and genotyping of tissue samples from genetically modified**
536 **mice**

537 The following mouse models of psychiatric disorders were examined for spine
538 nanostructural characteristics: male hemizygous or female homozygous neuroligin-3
539 R451C mutant (Nlgn3$^{R451C/(y\ or\ R451C)}$), heterozygous Syngap1 mutant mice (Syngap1$^{+/-}$),
540 heterozygous POGZ mutant mice (POGZ$^{Q1038R/+}$), mice with duplication of chromosome
541 7C (15q11-13$^{dup/+}$; corresponding to human 15q11-13 duplication), mice heterozygous
542 for deletion on chromosome 16B2,3 (3q29$^{del/+}$; corresponding to human 3q29 deletion),
543 mice heterozygous for deletion on chromosome 16qA13 (22q11.2$^{del/+}$; corresponding to
544 1.5 Mb deletion on human 22q11.2), mice heterozygous for Setd1a mutantion
545 (Setd1a$^{+/-}$), and Ca^{2+}/calmodulin-dependent protein kinase IIα kinase-dead mutant mice
546 (CaMKIIα$^{K42R/K42R}$). All animal experiments were reviewed and approved by the
547 Institutional Animal Care and Use Committee of the University of Tokyo (permission
548 number A2023M031-02).

549 For the production of embryos harboring heterozygous mutations, male heterozygous
550 mutants were bred with wild-type female C57BL/6J or C57BL/6N mice (Japan SLC).
551 Because neuronal cultures were prepared from wild-type and mutant littermates
552 sharing the same genetic background, differences between the C57BL/6J and
553 C57BL/6N sub-strains are unlikely to have affected the analysis. For the production of
554 Nlgn3$^{R451C/(y\ or\ R451C)}$ embryos, Nlgn3$^{R451C/y}$ males and Nlgn3$^{R451C/+}$ females were crossed.
555 Embryos of CaMKIIα$^{K42R/K42R}$ mice were obtained by crossing heterozygous
556 CaMKIIα$^{K42R/+}$ males and females. Both male and female embryos were used for the

557 primary culture. Control cultures were prepared from embryos without disease-related
558 mutations on the background of either C57BL/6J or C57BL/6N.
559 Genomic DNA was purified from E16 embryos prior to brain dissection using the
560 QuickGene DNA tissue kit (WAKO), and genotypes were determined by PCR using
561 either KapaTaq (Kapa Biosystems) or KOD FX Neo (TOYOBO) following the standard
562 protocols provided by the manufacturers. The primer sequences used for genotyping
563 were as follows:
564 Nlgn3$^{R451C/(y\ or\ R451C)}$ genotyping:
565 Sense primer: 5′- GGTCAGAGCTGTCATTGTCAC-3′
566 Antisense primer: 5’- TGTACCAGGAATGGGAAGCAG-3’
567 Syngap1$^{+/-}$ genotyping:
568 Sense primer for WT: 5’-GTCAGTGGGACATGGAAGTAG-3’
569 Sense primer for mutant: 5′-CTTCCTCGTGCTTTACGGTATC-3′
570 Antisense primer (common): 5’-CTGATCAGCCTGTCAGCAATG-3’
571 POGZ$^{Q1038R/+}$genotyping:
572 Sense primer for WT: 5’- TCTGTGAAGAAGCTTCGGGTAGTAC-3’
573 Antisense primer for WT: 5′-GTCTCCTCATTTACAGGGAGCT-3′
574 Sense primer for mutant: 5’- GCAGCGGCTCCCCGTTAAC-3’
575 Antisense primer for mutant: 5′- AGCGCACAGCCCACTCATAG-3′
576 15q11-13$^{dup/+}$ genotyping:
577 Sense primer: 5'- AGAGGAGGGCCTTACTAATTACTTA-3'
578 Antisense primer: 5′-ATATGTACTTTTGCATATAGTATAC -3′
579 3q29$^{del/+}$ genotyping:
580 Sense primer for WT: 5'- TTGGCACCACTCGCCCAAGTTATATCCACC-3'

581 Sense primer for mutant: 5’- CAAGGGGGAGGATTGGGAAGACAATAGCAG-3’

582 Antisense primer (common): 5’- GGTCATGCAAATTCTAGCAGTGAGTCATGAC-3’

583 22q11.2$^{del/+}$ genotyping:

584 Sense primer for WT: 5’- GAGAAAGTGGGTGGGAAGGC -3’

585 Antisense primer for WT: 5'- GTCCCTCGCCACAGTCATAA -3'

586 Sense primer for mutant: 5’- CTAAGGAATGGTTCCGGCCA -3’

587 Antisense primer for mutant: 5′- TTTCACGGAGGCGGTATTCA-3′

588 Setd1a$^{+/-}$ genotyping:

589 Sense primer: 5′-CTCGCCGCCATTTCTCTACATC-3′

590 Antisense primer: 5′-GTTCTGGAGGTTCTGGAGGTG-3′

591 CaMKIIα$^{K42R/K42R}$ genotyping:

592 Sense primer: 5’-GGTCTTGAAGACTGTCTGGTGTGAGA-3’

593 Antisense primer: 5′-CACAGGCCAGTTTAGGTCTTGCTAGG-3′

594

595 After genotyping, primary hippocampal neuron cultures were prepared from mutant and

596 corresponding control embryonic samples as described previously[12,62]. In brief, E16

597 hippocampi were dissected, minced, treated with trypsin (Gibco) and DNase (SIGMA),

598 and dissociated mechanically into a cell suspension. Cells were resuspended in

599 minimum essential medium supplemented with B18 supplement, L-glutamine (Gibco),

600 and 5% fetal calf serum (Equitech-Bio), and plated onto glass-bottom dishes (MatTek,

601 #1.5) precoated with poly-L-lysine (SIGMA). Glial proliferation was prevented by adding

602 5 μM Ara-C (SIGMA) 2 days after plating. For the comparison of spine nanostructure

603 between wild-type and mutant neurons, culture samples were processed for imaging at

604 18-22 DIV. For comparison of 8 mutant mouse models using SIM imaging, all imaging

605 data were obtained from the samples fixed at 19 DIV. For pharmacological treatment,
606 10 μM CNQX or 20 μM bicuculline was applied to the culture medium at 13 DIV, and
607 samples were processed for imaging at 19 DIV.
608
609 **Transfection and fluorescence labeling of primary hippocampal neurons**
610 Primary neurons were transfected with the indicated vectors using the calcium
611 phosphate precipitation method at 8–9 DIV according to a previously described
612 procedure[63]. All fluorescent proteins were expressed under the control of the β-actin
613 promoter.
614 The expression of the shRNA constructs was induced using the pSilencer vector
615 system. Briefly, the 19-nt target sequence and the reverse complement sequence of
616 the target were ligated into the shRNA expression vector separated by a 9-nt spacer
617 loop (TCTCTTGAA) (pSilencer 2.0-U6; Invitrogen). Stealth RNAi Negative Control
618 Duplexes (Invitrogen) were used as control shRNAs. The targeting sequences for
619 mouse Met, Arhgap15, and Ecrg4 are as follows:
620 Met RNAi sequence:
621 5’-GCAGTGAATTAGTTCGCTA-3
622 Arhgap15 RNAi sequence:
623 5’-AAGACAGATGTGAACATAC-3
624 Ecrg4 RNAi sequence:
625 5'- GAGGCTAAATTTGAAGAT-3'
626 The suppression of target protein expression by these transfected shRNAs was tested
627 by immunoblotting lysates of COS-7 cells co-transfected with a target gene construct
628 fused to a sequence encoding amino acids 98–106 of human influenza hemagglutinin

629 (HA), all under the control of the β-actin promoter. Overexpression of Cip4, Ecrg4, and
630 Npas4, genes upregulated in cultures derived from mouse models of schizophrenia,
631 was induced by transfection of plasmids containing the corresponding HA-fused cDNA
632 under the control of the β-actin promoter. Briefly, mouse Trip10 transcript variant 4
633 (Cip4; NM_001242391) and mouse Ecrg4 (NM_024283) were cloned, and an HA tag
634 was inserted into the C-termini. Mouse Npas4 (NM_153553) was cloned according to a
635 previous report[64] and fused with a Flag-HA tag at its C-terminus. Human neuropeptide
636 Y (NPY) tagged with green fluorescent protein (GFP, a kind gift from Dr. J. Takaska,
637 NIH) was expressed under the control of the β-actin promoter.
638 For cell surface labeling of individual neurons in culture, cells were fixed and stained
639 with 1,1'-dioctadecyl-3,3,3',3'-tetramethylindocarbocyanine perchlorate (DiI; Molecular
640 Probes) as described previously[12].
641
642 **Immunocytochemistry**
643 Cultured hippocampal neurons expressing HA-tagged constructs were fixed with 2%
644 paraformaldehyde in PBS, permeabilized with 0.2% Triton X-100 in PBS, blocked with
645 5% normal goat serum, and reacted with rabbit anti-HA antibody (1:500; MBL), mouse
646 anti-HA antibody (1:100; Biolegend), mouse anti-β-galactosidase antibody (1:500,
647 SIGMA), rabbit anti-Ecrg4 (1:100, SIGMA), mouse anti-GM130 antibody (1:100, BD
648 Biosciences), rabbit anti-Cip4/TRIP10 antibody (1:100, Proteintech), rabbit anti-NPAS4
649 antibody (1:100, Activity Signaling), and chicken anti-MAP2 antibody (1:500,
650 PhosphoSolutions). After washing with PBS, samples were reacted with Alexa Fluor
651 546-labeled goat anti-rabbit IgG antibody (1:500; Invitrogen) and Alexa Fluor 647-
652 labeled goat anti-mouse IgG antibody or anti-chicken IgY antibodies (1:500;

653 Invitrogen). For cell surface labeling with GFP, neurons expressing Ecrg4-HA-SEP
654 (superecliptic pHluorin) were reacted with anti-GFP VHH/nanobody conjugated to
655 Alexa Fluor 647 (1:4,000; Chromotek) in culture medium at 37°C.
656
657 **Structured illumination microscopy (SIM) imaging**
658 For 3D-SIM imaging, we used an inverted microscope (ECLIPSE Ti-E, NIKON)
659 equipped with an N-SIM-E system, 405, 488, 561, and 640 nm diode lasers (LU-NV,
660 NIKON), and an oil-immersion TIRF objective lens (SR Apo TIRF 100 ×, N.A. 1.49,
661 NIKON). All SIM images were acquired under strictly controlled conditions, including a
662 stage temperature of 28–29°C, to minimize the position and aberration fluctuations.
663 Spherical aberrations induced by refractive index mismatch were reduced by manually
664 adjusting the objective lens correction collar. Images were acquired using an EMCCD
665 camera (iXon3 DU-897E, Andor Technology) with 512 × 512 pixels (each pixel, 16 μm
666 square) operated in the read-out mode at 1 MHz with 16-bit analog-to-digital
667 conversion of the EM gain. All image-processing steps were performed in three
668 dimensions. The acquired image datasets were computationally reconstructed using
669 the reconstruction stack algorithm V2.10 of NIS-Elements AR (NIKON). An image stack
670 consisted of 63 axial (z) planes of 512 × 512 pixels in the x- and y-dimensions, with a
671 pixel size of 32 × 32 nm. All 3D images were reconstructed in 120-nm z-steps spanning
672 7.56 μm in the z-axis. The voxel size met the Nyquist criterion. Only dendritic segments
673 spatially isolated from other fluorescent objects were selected for analysis because
674 objects brighter than the targeted dendritic segments made image thresholding
675 unreliable. Quality checks of the acquired SIM images were performed as described
676 previously using the SIMcheck plugin for ImageJ[65].

677

678 **Spine isolation and shape measurement**

679 Spines were isolated by automated image thresholding using a previously described
680 method[12]. Briefly, the reconstructed SIM image stacks were first processed by
681 multilevel thresholding using the MATLAB built-in function [multithresh()] to produce
682 binary images, which were further processed by geodesic active contours using the
683 MATLAB built-in function [activecontour()]. The binary image stacks generated by
684 thresholding the SIM images were then processed for the automated detection of
685 spines. First, the dendritic shafts were fitted with elliptic cylinders and voxel clusters
686 outside the best-fit elliptic cylinders were identified as spine candidates. Next, the spine
687 candidates were classified by volume and shape. After selection, the junction between
688 the dendritic shaft and spine was determined. Finally, the nanostructural parameters of
689 isolated spines were measured. These steps are basically the same as those in our
690 previous algorithm, but several points were improved, as described in the following
691 sections (The original code for SIM image processing is available at
692 https://shigeookabe.github.io/download-page-SIM/
693 with a password of "simspineimage").

694

695 (1) Dendritic shaft fitting

696 We first estimated the shaft volume using the custom-made function "SIM_Fitdendrite"
697 as previously described. In the new algorithm, the candidate spines were subsequently
698 evaluated to determine whether their bases were large and spread on the shaft
699 surface. If the spine base was large, the basal voxels were removed using the function
700 "SIM_Removevoxel."

(2) Selection of the spines

Using the custom-made function "SIM_Position," spines with volumes too small, too elongated, or located at the image edge were removed as previously described. Small spine candidates with volumes less than twice the volume of a rectangular cuboid with edge lengths equal to the theoretical resolutions of SIM images (<0.01 μm^3) were rejected.

(3) Adjustment of the spine–shaft junction

We determined the location of spine–shaft junction using the custom-made function "SIM_Junction." This step was identical to our previous algorithm. Next, spines with more than one connection site to the shaft were detected using the function "SIM_Neck" and eliminated from further analysis.

(4) Measurement of nanostructural parameters

First, the angle of the spines was adjusted to be perpendicular to the long axis of the dendritic shaft and within the xy-plane using the function "SIM_Angle." Next, nanostructural parameters were measured using the function "SIM_Shape." In our previous spine shape measurement study, a polygon mesh-based calculation was performed. In the current study, we took a different approach using voxel-based measurement. The calculation of structural parameters using voxel data was more straightforward and required fewer calculation steps than the method based on polygon mesh data. Spines were divided into 160-nm segments along the long axis using the function "SIM_Shape." These spine segments were used to calculate the following 64 nanostructural parameters: spine length, surface area, base surface area, total volume, volume of each spine segment (20 segments), convex hull volume of each spine segment (20 segments), and convex hull ratio of each spine segment (20 segments).

725

726 **Analysis of the spine population data**

727 Differences in spine phenotype among model mice were analyzed at the population
728 level by PCA. We selected five parameters (spine length, base surface, total volume,
729 and volumes of the fifth and fifteenth spine segments) for the PCA-based dimensional
730 reduction. Two parameters that reflect the principal structural features (length and
731 volume) were first selected. Second, three other parameters (base surface, volumes of
732 the fifth and fifteenth spine segments) that were mutually independent and also
733 independent from the first two parameters were chosen (pairwise correlation
734 coefficients < 0.3). The initial 64 parameters included the volume of each spine
735 segment (20 segments), the convex hull volume of each spine segment (20 segments),
736 and the convex hull ratio of each spine segment (20 segments). These parameters
737 showed higher correlation coefficients but did not improve PCA performance. We also
738 confirmed that PCA using all 64 parameters yields a cross-correlation map similar to
739 that shown in Fig. 2B. The first three principal components (PC1–PC3) covered
740 approximately 90% of the variance in the data.

741 The 2D presentation of spine population data using PC1 and PC2 reflected the overall
742 pattern of the spine shape distribution, with thin, mushroom, and stubby spines
743 separated in the feature space. We found that the overall pattern of spine population
744 data projected to the PC1-PC2 plane differs between DiI-labeled neurons and GFP-
745 expressing neurons. This difference may be due to the properties of SIM images
746 obtained from either cell-surface labeling or cytoplasmic GFP expression. To facilitate
747 the direct comparison of the spine population data in Figure 3 (DiI-labeled neurons)
748 and Figure 8 (GFP-expressing neurons), we transformed the raw data of GFP-

749 expressing neurons using the weight matrix calculated from the data for DiI-labeled
750 neurons.
751 After PCA, relative spine densities (spine number per area in the feature space) were
752 mapped onto an 80 × 80 grid spanning ±4 standard deviations along PC1 and PC2.
753 Using this procedure, two density plots were generated: one from culture samples of
754 disease model mice and the other from corresponding control cultures. The two density
755 plots were then subtracted to extract the local differences in spine numbers. Because
756 each grid contains spines with similar structural parameters, the subtracted plot reveals
757 regions of mutant-dominant and wild-type-dominant spine distributions in the PC1–PC2
758 plane.
759 The similarity between the two subtracted density plots was evaluated by calculating
760 the 2D cross-correlation C using the following equation
761
762 $$C = \frac{\sum_{m=1}^{M}\sum_{n=1}^{N} X(m,n)Y(m,n)}{\sqrt{\sum_{m=1}^{M}\sum_{n=1}^{N} X(m,n)X(m,n)}\sqrt{\sum_{m=1}^{M}\sum_{n=1}^{N} Y(m,n)Y(m,n)}},$$
763
764 where X and Y correspond to the two subtracted density matrices. The 11 different
765 subtracted density plots shown in Figure 2 were clustered using the MATLAB function
766 "linkage," and the average distance between all pairs of elements in the two samples
767 was calculated using the cluster algorithm.
768 For Figure 3, the PC1–PC2 feature space was divided into four subareas with distinct
769 shape properties: (1) small and short, (2) small and long, (3) large and short, and (4)
770 large and long. The median spine volume and length were first calculated from the
771 wild-type population, and spine samples were classified into four subgroups based on
772 these median values. Each position of the 80 × 80 grid was then labeled according to

773 the dominant subgroup of spines it contained, yielding a map of four subareas
774 corresponding to the four spine shape categories.
775 In Figure 3, 8, and Supplementary Figure 3, areas in the feature space enriched with
776 mutant or control spines were extracted by searching the 80 × 80 grid and identifying
777 those where the difference in relative density was larger than the mean plus 3 × SD.
778 Spine axial profiles in Supplementary Figure 5 were then analyzed within areas
779 enriched with either mutant or control spines.
780
781 **Time-lapse imaging of dendritic spines and image analysis**
782 Live cell 3D imaging was performed using an A1 confocal laser scanning microscope
783 (NIKON) equipped with 405, 488, 561, and 640 nm diode lasers (LU-NV, NIKON). Cells
784 at 15–18 DIV were maintained at 37°C under a continuous flow of 5% CO_2 to maintain
785 medium pH using a heater stage system (INUG2H-TIZSH, Tokai Hit) with a lid
786 designed for a glass-bottom dish to minimize evaporation. Horizontal and vertical drifts
787 were controlled by a motorized stage and a perfect focus system, respectively. Images
788 were acquired with an oil immersion objective lens (60×, NA 1.4, NIKON) at a confocal
789 aperture of 1 AU. The imaged volume was 30.7 × 30.7 × 7.56 μm in x, y, and z
790 directions, respectively, and image stacks consisted of 17 planes separated by 500 nm.
791 Time-lapse images were recorded either at short intervals (15 min intervals for 24 h) or
792 long intervals (two time points separated by 24 h). Cultured neurons imaged at a 24-h
793 interval were then fixed and immunostained with anti-HA to confirm the expression
794 levels of the transfected genes. The effect of exogenously applied Ecrg4 peptide
795 (CΔ16; the C-terminal ECRG4 fragment of 16 aa, 5.4 μM, BEX CO., LTD.) was

796 evaluated by taking time-lapse images at 24 h intervals, with the first image taken just
797 before the peptide application.
798 The image stacks obtained by time-lapse imaging were analyzed using custom-made
799 MATLAB scripts. First, 2D images were generated by maximal intensity projection of z-
800 stack images. These 2D images were processed to transform the outlines of dendritic
801 shafts to be aligned with straight lines. Spines were subsequently identified as objects
802 extending beyond the straight edges of the dendritic shafts. Identified spines were
803 segmented, and total fluorescence intensities were measured as a proxy for spine
804 volume. We classified the spines as stable (present throughout the imaging period),
805 newly formed (appearing within 24 h imaging period), and eliminated (lost within 24 h
806 imaging period). For newly formed and eliminated spines, we generated temporal
807 profiles of growth and shrinkage using the total fluorescence intensity values.
808
809 **RNA sequencing and gene expression analysis**
810 Total RNA was isolated from cultured hippocampal neurons at 19 DIV using the
811 RNeasy Mini Kit (QIAGEN) with the RNase-Free DNase Set (QIAGEN) according to
812 the manufacturer's protocols. The quality of the extracted RNA was initially assessed
813 using a NanoDrop spectrophotometer, and the RNA integrity number (RIN) score was
814 calculated for each sample using a Bioanalyzer (Agilent Technologies). The yields were
815 quantified using a Qubit Fluorometer (Thermo Fisher Scientific). Sequencing libraries
816 were prepared using the NEBNext Ultra Directional RNA Library Prep Kit for directional
817 libraries (New England BioLabs) and the KAPA HTP Library Preparation Kit (KAPA
818 Biosystems) according to the manufacturers' protocols. Paired-end RNA-seq libraries
819 were sequenced using the Illumina HiSeq and MGI DNBSEQ-G400 platforms. Three

820 independent culture preparations were used for RNA sequencing of each mouse model
821 and control library. Following quality control, the reads were aligned with the mouse
822 reference genome GRCm38/mm10 (GenBank assembly ID: GCA_000001635.2).
823 Expression levels of genes were analyzed based on the transcripts per million and
824 differential expression analysis was conducted using the DESeq2 package in R[66].
825 Differentially expressed genes (DEGs) were selected according to an adjusted $P <$
826 0.05 and a (log2)-fold change greater than 0.5.
827
828 **Simulation of spine development**
829 Spine growth was simulated using a dendrite model consisting of 1,000 segments,
830 each 0.25 μm in length (250 μm in total). The spine distribution was updated every 20
831 min over 10 days, covering the initial phase of spine development from 8 DIV to 17
832 DIV. The initial probability of new spine generation was set at 7.5×10^{-3} per segment
833 per hour and decreased thereafter in proportion to the accrued spine density increase
834 (by the final 24 h, the probability of spine generation [mean ± SD] was $3.2 \times 10^{-3} \pm 0.23$
835 $\times 10^{-3}$/segment/h). This probability function yielded an average of 1.2 ± 0.22 new
836 spines per 10 μm of dendrite every 24 h, in good agreement with the spine dynamics
837 measured by time-lapse imaging from 15–18 DIV (1.3 ± 0.63 new spines per 10 μm of
838 dendrite every 24 h). The model also set the increase in spine volume (V1) from $6.7 \times$
839 10^{-3} to 3.3×10^{-2} in 20 min. Spines in the early growth phase were treated as unstable,
840 with loss probability P1 ranging from 9.0×10^{-3} to 0.1 every 20 min. Spines were
841 modeled as stabilized when the individual volume reached a relative value of 1.0.
842 These stabilized spines then entered a shrinking phase with a probability P2 ranging
843 from 2.9×10^{-3} to 4.0×10^{-3} in 20 min. The shrinking rate V2 was set from 6.7×10^{-3} to

844 3.3×10^{-2} per 20 min. In simulations, the four parameters V1, V2, P1, and P2 were
845 varied within these indicated ranges to find the combination producing the best fit with
846 experimental data on the difference in spine lifetime distribution profile and turnover
847 rate at 24 h (the actual measurement interval). The simulation with the best-fit
848 parameters yielded a spine density comparable to measured data (0.57 ± 0.029 vs.
849 0.70 ± 0.17 spines/μm of dendrite).
850
851 **Western blotting**
852 Total protein extracts from cultured hippocampal neurons were separated into cytosolic
853 and membrane fractions using Trident Membrane Protein Extraction Kit (GeneTex)
854 according to the manufacturer's protocol and separated on 10% sodium dodecyl sulfate
855 (SDS)-polyacrylamide gels or 15%–20% Tricine-SDS-polyacrylamide gels. The
856 separated proteins were then transferred onto nitrocellulose membranes (Millipore) or
857 PVDF membranes (Bio-Rad) using a wet transfer system. Membranes were blocked
858 with 5% bovine serum albumin in Tris-buffered saline plus Tween-20 (TBS-T, 20 mM
859 Tris-HCl, 137 mM NaCl, 0.2% Tween-20) for 1 h at room temperature, then incubated
860 overnight at 4°C with rabbit anti-Ecrg4 (1:1,000, SIGMA), rabbit anti-GluA1 (1:1,000,
861 Nittobo Medical), rabbit anti-GFP (1:3,000, MBL), rabbit anti-dsRed2 (1:4,000, Nittobo
862 Medical), mouse anti-α-tubulin (1:3,000, SIGMA) as indicated. The membranes were
863 washed and incubated with HRP-conjugated secondary antibody against mouse or
864 rabbit IgG (1:10,000, Amersham) for 2 h. Signals from the target protein bands were
865 detected using a SuperSignal™ West Femto or Atto detection kit (Pierce) and imaged
866 for quantitation (densitometry) using a ChemiDoc imaging system (Bio-Rad). We
867 isolated the fraction of synaptosomes using Syn-PER™ Synaptic Protein Extraction

868 Reagent (Thermo Scientific) in Supplementary Figure 9A, according to the
869 manufacture's protocols.
870
871 **Statistics**
872 The statistical tests used for each experiment and the sample sizes (spines, dendrites,
873 cells, and plates) are indicated in the corresponding text or figure legends. Statistical
874 significance was determined as follows:
875 Figure 3G-J: One-way ANOVA followed by Tukey's post hoc test.
876 Figure 5A-C: A linear mixed-effects model with genotype as a fixed effect and plate,
877 cell, and dendrite as nested random effects.
878 Figure 5D-F: A linear mixed-effects model with genotype as a fixed effect and plate,
879 cell, dendrite, and spine as nested random effects.
880 Figure 5G-L: A linear mixed-effects model with genotype as a fixed effect and plate,
881 cell, dendrite, spine, and time as nested random effects.
882 Figure 7A: A linear mixed-effects model with treatment as a fixed effect and plate, cell,
883 and dendrite as nested random effects.
884 Figure 8: Three independent imaging datasets evaluated by permutation tests.
885 Statistical significance was set at $P < 0.05$.
886

887 **Acknowledgments**

888 We thank Toru Takumi for the 15q11-13$^{dup/+}$ mice, Katsuhiko Tabuchi for Nlgn3$^{R451C/(y\ or}$
889 $^{R451C)}$ mice, Yoko Yamagata for CaMKIIα$^{K42R/K42R}$ mice, and Justin Taraska for the NPY
890 tagged with GFP. This work was supported by Grants-in-Aid for Scientific Research
891 (25H01038, 20H00481, 20H05894, 20H05895 to S.O.), the Japan Agency for Medical
892 Research and Development (JP19gm1310003 to S.O., T. N., and Y. G.,
893 JP22jm0210097, JP25wm0625001h0003 to S.O., JP19dm0207071 to A. A.), the Naito
894 Foundation, and the Uehara Memorial Foundation.

895 **Author contributions**

896 Y.K. and S.O. conceived of the project and designed the methodology. Y.K. and Q.L.
897 performed the experiments. R. S., A.A. and T.N. provided the animal resources and
898 provided advice on analysis. Y.G. conducted the gene expression analysis. S.O. and
899 Y.K. wrote the manuscript, with contributions from A.A., T.N., and Y.G.

900 **Declarations of interests**

901 The authors declare no competing interests. Additional affiliation of the authors is as
902 follows; Shigeo Okabe; Director, RIKEN Center for Brain Science.

903 **Declarations of generative AI and AI-assisted technologies in the writing process**

904 The authors utilized Grammarly (https://app.grammarly.com/) for editing the text. The
905 authors take full responsibility for the contents of the manuscript.

906 **Resource availability**

907 The original code for SIM image processing is available at
908 https://shigeookabe.github.io/download-page-SIM/
909 with a password of "simspineimage".
910

References

1. Rochefort, N.L., and Konnerth, A. (2012). Dendritic spines: from structure to in vivo function. EMBO Rep. *13*, 699–708. https://doi.org/10.1038/EMBOR.2012.102.
2. Sala, C., and Segal, M. (2014). Dendritic spines: the locus of structural and functional plasticity. Physiol. Rev. *94*, 141–188. https://doi.org/10.1152/physrev.00012.2013.
3. Matsuzaki, M., Ellis-Davies, G.C.R., Nemoto, T., Miyashita, Y., Iino, M., and Kasai, H. (2001). Dendritic spine geometry is critical for AMPA receptor expression in hippocampal CA1 pyramidal neurons. Nat. Neurosci. *4*, 1086–1092. https://doi.org/10.1038/NN736.
4. Matsuzaki, M., Honkura, N., Ellis-Davies, G.C.R., and Kasai, H. (2004). Structural basis of long-term potentiation in single dendritic spines. Nature *429*, 761–766. https://doi.org/10.1038/nature02617.
5. Nägerl, U.V., Eberhorn, N., Cambridge, S.B., and Bonhoeffer, T. (2004). Bidirectional activity-dependent morphological plasticity in hippocampal neurons. Neuron *44*, 759–767. https://doi.org/10.1016/j.neuron.2004.11.016.
6. Zhou, Q., Homma, K.J., and Poo, M.M. (2004). Shrinkage of dendritic spines associated with long-term depression of hippocampal synapses. Neuron *44*, 749–757. https://doi.org/10.1016/j.neuron.2004.11.011.
7. Loewenstein, Y., Kuras, A., and Rumpel, S. (2011). Multiplicative dynamics underlie the emergence of the log-normal distribution of spine sizes in the neocortex in vivo. Journal of Neuroscience *31*, 9481–9488. https://doi.org/10.1523/JNEUROSCI.6130-10.2011.
8. Loewenstein, Y., Yanover, U., and Rumpel, S. (2015). Predicting the dynamics of network connectivity in the neocortex. Journal of Neuroscience *35*, 12535–12544. https://doi.org/10.1523/JNEUROSCI.2917-14.2015.
9. Statman, A., Kaufman, M., Minerbi, A., Ziv, N.E., and Brenner, N. (2014). Synaptic size dynamics as an effectively stochastic process. PLoS Comput. Biol. *10*. https://doi.org/10.1371/JOURNAL.PCBI.1003846.
10. Hazan, L., and Ziv, N.E. (2020). Activity dependent and independent determinants of synaptic size diversity. J. Neurosci. *40*, 2828–2848. https://doi.org/10.1523/JNEUROSCI.2181-19.2020.
11. Tønnesen, J., Katona, G., Rózsa, B., and Nägerl, U.V. (2014). Spine neck plasticity regulates compartmentalization of synapses. Nat. Neurosci. *17*, 678–685. https://doi.org/10.1038/nn.3682.

12. Kashiwagi, Y., Higashi, T., Obashi, K., Sato, Y., Komiyama, N.H., Grant, S.G.N., and Okabe, S. (2019). Computational geometry analysis of dendritic spines by structured illumination microscopy. Nat. Commun. *10*, 1285. https://doi.org/10.1038/s41467-019-09337-0.
13. Zaccard, C.R., Shapiro, L., Martin-de-Saavedra, M.D., Pratt, C., Myczek, K., Song, A., Forrest, M.P., and Penzes, P. (2020). Rapid 3D enhanced resolution microscopy reveals diversity in dendritic spinule dynamics, regulation, and function. Neuron *107*, 522–537. https://doi.org/10.1016/j.neuron.2020.04.025.
14. Penzes, P., Cahill, M.E., Jones, K.A., VanLeeuwen, J.-E., and Woolfrey, K.M. (2011). Dendritic spine pathology in neuropsychiatric disorders. Nat. Neurosci. *14*, 285–293. https://doi.org/10.1038/nn.2741.
15. Fromer, M., Pocklington, A.J., Kavanagh, D.H., Williams, H.J., Dwyer, S., Gormley, P., Georgieva, L., Rees, E., Palta, P., Ruderfer, D.M., et al. (2014). De novo mutations in schizophrenia implicate synaptic networks. Nature *506*, 179–184. https://doi.org/10.1038/NATURE12929.
16. Rodriguez-Murillo, L., Gogos, J.A., and Karayiorgou, M. (2012). The genetic architecture of schizophrenia: new mutations and emerging paradigms. Annu. Rev. Med. *63*, 63–80. https://doi.org/10.1146/ANNUREV-MED-072010-091100.
17. Gulsuner, S., Walsh, T., Watts, A.C., Lee, M.K., Thornton, A.M., Casadei, S., Rippey, C., Shahin, H., Nimgaonkar, V.L., Go, R.C.P., et al. (2013). Spatial and temporal mapping of de novo mutations in schizophrenia to a fetal prefrontal cortical network. Cell *154*, 518–529. https://doi.org/10.1016/J.CELL.2013.06.049.
18. Bourgeron, T. (2015). From the genetic architecture to synaptic plasticity in autism spectrum disorder. Nat. Rev. Neurosci. *16*, 551–563. https://doi.org/10.1038/NRN3992.
19. Terashima, H., Minatohara, K., Maruoka, H., and Okabe, S. (2022). Imaging neural circuit pathology of autism spectrum disorders: autism-associated genes, animal models and the application of in vivo two-photon imaging. Microscopy (Oxf). *71*, I81–I99. https://doi.org/10.1093/JMICRO/DFAB039.
20. Zieger, H.L., and Choquet, D. (2021). Nanoscale synapse organization and dysfunction in neurodevelopmental disorders. Neurobiol. Dis. *158*, 105453. https://doi.org/10.1016/J.NBD.2021.105453.
21. Yilmaz, M., Yalcin, E., Presumey, J., Aw, E., Ma, M., Whelan, C.W., Stevens, B., McCarroll, S.A., and Carroll, M.C. (2021). Overexpression of schizophrenia susceptibility factor human complement C4A promotes excessive synaptic loss and behavioral changes in mice. Nat. Neurosci. *24*, 214–224.

983 https://doi.org/10.1038/S41593-020-00763-8.
984 22. Obi-Nagata, K., Suzuki, N., Miyake, R., MacDonald, M.L., Fish, K.N., Ozawa, K.,
985 Nagahama, K., Okimura, T., Tanaka, S., Kano, M., et al. (2023). Distorted
986 neurocomputation by a small number of extra-large spines in psychiatric disorders.
987 Sci. Adv. *9*, eade5973. https://doi.org/10.1126/SCIADV.ADE5973.
988 23. Mukai, J., Dhilla, A., Drew, L.J., Stark, K.L., Cao, L., MacDermott, A.B.,
989 Karayiorgou, M., and Gogos, J.A. (2008). Palmitoylation-dependent
990 neurodevelopmental deficits in a mouse model of 22q11 microdeletion. Nat.
991 Neurosci. *11*, 1302–1310. https://doi.org/10.1038/nn.2204.
992 24. Nakai, N., Takumi, T., Nakai, J., and Sato, M. (2018). Common defects of spine
993 dynamics and circuit function in neurodevelopmental disorders: A systematic
994 review of findings from in vivo optical imaging of mouse models. Front. Neurosci.
995 *12*. https://doi.org/10.3389/FNINS.2018.00412/PDF.
996 25. Shcheglovitov, A., Shcheglovitova, O., Yazawa, M., Portmann, T., Shu, R.,
997 Sebastiano, V., Krawisz, A., Froehlich, W., Bernstein, J.A., Hallmayer, J.F., et al.
998 (2013). SHANK3 and IGF1 restore synaptic deficits in neurons from 22q13
999 deletion syndrome patients. Nature *503*, 267–271.
1000 https://doi.org/10.1038/NATURE12618.
1001 26. Llamosas, N., Arora, V., Vij, R., Kilinc, M., Bijoch, L., Rojas, C., Reich, A.,
1002 Sridharan, B.P., Willems, E., Piper, D.R., et al. (2020). SYNGAP1 controls the
1003 maturation of dendrites, synaptic function, and network activity in developing
1004 human neurons. J. Neurosci. *40*, 7980–7994.
1005 https://doi.org/10.1523/JNEUROSCI.1367-20.2020.
1006 27. Yamamoto, K., Kuriu, T., Matsumura, K., Nagayasu, K., Tsurusaki, Y., Miyake, N.,
1007 Yamamori, H., Yasuda, Y., Fujimoto, M., Fujiwara, M., et al. (2021). Multiple
1008 alterations in glutamatergic transmission and dopamine D2 receptor splicing in
1009 induced pluripotent stem cell-derived neurons from patients with familial
1010 schizophrenia. Transl. Psychiatry *11*, 548. https://doi.org/10.1038/S41398-021-
1011 01676-1.
1012 28. Wen, Z., Nguyen, H.N., Guo, Z., Lalli, M.A., Wang, X., Su, Y., Kim, N.S., Yoon,
1013 K.J., Shin, J., Zhang, C., et al. (2014). Synaptic dysregulation in a human iPS cell
1014 model of mental disorders. Nature *515*, 414–418.
1015 https://doi.org/10.1038/NATURE13716.
1016 29. Chisholm, K., Lin, A., Abu-Akel, A., and Wood, S.J. (2015). The association
1017 between autism and schizophrenia spectrum disorders: A review of eight alternate
1018 models of co-occurrence. Neurosci. Biobehav. Rev. *55*, 173–183.

https://doi.org/10.1016/J.NEUBIOREV.2015.04.012.

30. De Crescenzo, F., Postorino, V., Siracusano, M., Riccioni, A., Armando, M., Curatolo, P., and Mazzone, L. (2019). Autistic symptoms in schizophrenia spectrum disorders: A systematic review and meta-analysis. Front. Psychiatry *10*. https://doi.org/10.3389/FPSYT.2019.00078/PDF.

31. Nenadić, I., Meller, T., Evermann, U., Schmitt, S., Pfarr, J.K., Abu-Akel, A., and Grezellschak, S. (2021). Subclinical schizotypal vs. autistic traits show overlapping and diametrically opposed facets in a non-clinical population. Schizophr. Res. *231*, 32–41. https://doi.org/10.1016/J.SCHRES.2021.02.018.

32. Crespi, B., and Badcock, C. (2008). Psychosis and autism as diametrical disorders of the social brain. Behav. Brain Sci. *31*, 241–261. https://doi.org/10.1017/S0140525X08004214.

33. Pratt, J., Winchester, C., Dawson, N., and Morris, B. (2012). Advancing schizophrenia drug discovery: optimizing rodent models to bridge the translational gap. Nat. Rev. Drug Discov. *11*, 560–570. https://doi.org/10.1038/NRD3649.

34. Isshiki, M., Tanaka, S., Kuriu, T., Tabuchi, K., Takumi, T., and Okabe, S. (2014). Enhanced synapse remodelling as a common phenotype in mouse models of autism. Nat. Commun. *5*, 4742. https://doi.org/10.1038/ncomms5742.

35. Lee, E., Lee, J., and Kim, E. (2017). Excitation/inhibition imbalance in animal models of autism spectrum disorders. Biol. Psychiatry *81*, 838–847. https://doi.org/10.1016/J.BIOPSYCH.2016.05.011.

36. Tabuchi, K., Blundell, J., Etherton, M.R., Hammer, R.E., Liu, X., Powell, C.M., and Südhof, T.C. (2007). A neuroligin-3 mutation implicated in autism increases inhibitory synaptic transmission in mice. Science *318*, 71–76. https://doi.org/10.1126/science.1146221.

37. Etherton, M., Földy, C., Sharma, M., Tabuchi, K., Liu, X., Shamloo, M., Malenka, R.C., and Südhof, T.C. (2011). Autism-linked neuroligin-3 R451C mutation differentially alters hippocampal and cortical synaptic function. Proc. Natl. Acad. Sci. U. S. A. *108*, 13764–13769. https://doi.org/10.1073/pnas.1111093108.

38. Komiyama, N.H., Watabe, A.M., Carlisle, H.J., Porter, K., Charlesworth, P., Monti, J., Strathdee, D.J.C., O'Carroll, C.M., Martin, S.J., Morris, R.G.M., et al. (2002). SynGAP regulates ERK/MAPK signaling, synaptic plasticity, and learning in the complex with postsynaptic density 95 and NMDA receptor. The Journal of Neuroscience *22*, 9721–9732. https://doi.org/22/22/9721 [pii].

39. Matsumura, K., Seiriki, K., Okada, S., Nagase, M., Ayabe, S., Yamada, I., Furuse, T., Shibuya, H., Yasuda, Y., Yamamori, H., et al. (2020). Pathogenic POGZ

1055 mutation causes impaired cortical development and reversible autism-like
1056 phenotypes. Nat. Commun. *11*, 859. https://doi.org/10.1038/s41467-020-14697-z.
1057 40. Nakatani, J., Tamada, K., Hatanaka, F., Ise, S., Ohta, H., Inoue, K., Tomonaga, S.,
1058 Watanabe, Y., Chung, Y.J., Banerjee, R., et al. (2009). Abnormal behavior in a
1059 chromosome- engineered mouse model for human 15q11-13 duplication seen in
1060 autism. Cell *137*, 1235–1246. https://doi.org/10.1016/j.cell.2009.04.024.
1061 41. Baba, M., Yokoyama, K., Seiriki, K., Naka, Y., Matsumura, K., Kondo, M.,
1062 Yamamoto, K., Hayashida, M., Kasai, A., Ago, Y., et al. (2019). Psychiatric-
1063 disorder-related behavioral phenotypes and cortical hyperactivity in a mouse
1064 model of 3q29 deletion syndrome. Neuropsychopharmacology *44*, 2125–2135.
1065 https://doi.org/10.1038/s41386-019-0441-5.
1066 42. Saito, R., Miyoshi, C., Koebis, M., Kushima, I., Nakao, K., Mori, D., Ozaki, N.,
1067 Funato, H., Yanagisawa, M., and Aiba, A. (2021). Two novel mouse models
1068 mimicking minor deletions in 22q11.2 deletion syndrome revealed the contribution
1069 of each deleted region to psychiatric disorders. Mol. Brain *14*.
1070 https://doi.org/10.1186/S13041-021-00778-7.
1071 43. Nagahama, K., Sakoori, K., Watanabe, T., Kishi, Y., Kawaji, K., Koebis, M., Nakao,
1072 K., Gotoh, Y., Aiba, A., Uesaka, N., et al. (2020). Setd1a insufficiency in mice
1073 attenuates excitatory synaptic function and recapitulates schizophrenia-related
1074 behavioral abnormalities. Cell Rep. *32*, 108126.
1075 https://doi.org/10.1016/J.CELREP.2020.108126.
1076 44. Yamagata, Y., Kobayashi, S., Umeda, T., Inoue, A., Sakagami, H., Fukaya, M.,
1077 Watanabe, M., Hatanaka, N., Totsuka, M., Yagi, T., et al. (2009). Kinase-dead
1078 knock-in mouse reveals an essential role of kinase activity of Ca^{2+}/calmodulin-
1079 dependent protein kinase IIα in dendritic spine enlargement, long-term
1080 potentiation, and learning. Journal of Neuroscience *29*, 7607–7618.
1081 https://doi.org/10.1523/JNEUROSCI.0707-09.2009.
1082 45. Yamasaki, N., Maekawa, M., Kobayashi, K., Kajii, Y., Maeda, J., Soma, M., Takao,
1083 K., Tanda, K., Ohira, K., Toyama, K., et al. (2008). Alpha-CaMKII deficiency causes
1084 immature dentate gyrus, a novel candidate endophenotype of psychiatric
1085 disorders. Mol. Brain *1*, 6. https://doi.org/10.1186/1756-6606-1-6.
1086 46. Featherstone, R.E., Shimada, T., Crown, L.M., Melnychenko, O., Yi, J.,
1087 Matsumoto, M., Tajinda, K., Mihara, T., Adachi, M., and Siegel, S.J. (2022).
1088 Calcium/calmodulin-dependent protein kinase IIα heterozygous knockout mice
1089 show electroencephalogram and behavioral changes characteristic of a
1090 subpopulation of schizophrenia and intellectual impairment. Neuroscience *499*,

104–117. https://doi.org/10.1016/J.NEUROSCIENCE.2022.07.023.

47. Stephenson, J.R., Wang, X., Perfitt, T.L., Parrish, W.P., Shonesy, B.C., Marks, C.R., Mortlock, D.P., Nakagawa, T., Sutcliffe, J.S., and Colbran, R.J. (2017). A Novel Human CAMK2A Mutation Disrupts Dendritic Morphology and Synaptic Transmission, and Causes ASD-Related Behaviors. J. Neurosci. *37*, 2216–2233. https://doi.org/10.1523/JNEUROSCI.2068-16.2017.

48. Brown, C.N., Cook, S.G., Allen, H.F., Crosby, K.C., Singh, T., Coultrap, S.J., and Bayer, K.U. (2021). Characterization of six CaMKIIα variants found in patients with schizophrenia. iScience *24*. https://doi.org/10.1016/j.isci.2021.103184.

49. Qiu, S., Lu, Z., and Levitt, P. (2014). MET receptor tyrosine kinase controls dendritic complexity, spine morphogenesis, and glutamatergic synapse maturation in the hippocampus. J. Neurosci. *34*, 16166–16179. https://doi.org/10.1523/JNEUROSCI.2580-14.2014.

50. Bloodgood, B.L., Sharma, N., Browne, H.A., Trepman, A.Z., and Greenberg, M.E. (2013). The activity-dependent transcription factor NPAS4 regulates domain-specific inhibition. Nature *503*, 121–125. https://doi.org/10.1038/nature12743.

51. Spiegel, I., Mardinly, A.R., Gabel, H.W., Bazinet, J.E., Couch, C.H., Tzeng, C.P., Harmin, D.A., and Greenberg, M.E. (2014). Npas4 regulates excitatory-inhibitory balance within neural circuits through cell-type-specific gene programs. Cell *157*, 1216–1229. https://doi.org/10.1016/J.CELL.2014.03.058.

52. Zamboni, V., Armentano, M., Saró, G., Ciraolo, E., Ghigo, A., Germena, G., Umbach, A., Valnegri, P., Passafaro, M., Carabelli, V., et al. (2016). Disruption of ArhGAP15 results in hyperactive Rac1, affects the architecture and function of hippocampal inhibitory neurons and causes cognitive deficits. Sci. Rep. *6*. https://doi.org/10.1038/SREP34877.

53. Ba, W., Selten, M.M., van der Raadt, J., van Veen, H., Li, L.L., Benevento, M., Oudakker, A.R., Lasabuda, R.S.E., Letteboer, S.J., Roepman, R., et al. (2016). ARHGAP12 functions as a developmental brake on excitatory synapse function. Cell Rep. *14*, 1355–1368. https://doi.org/10.1016/J.CELREP.2016.01.037.

54. Nakatani, Y., Kiyonari, H., and Kondo, T. (2019). Ecrg4 deficiency extends the replicative capacity of neural stem cells in a Foxg1-dependent manner. Development *146*, dev168120. https://doi.org/10.1242/DEV.168120.

55. Richter, M., Lalli, E., and Ruggiero, C. (2023). Complex and pleiotropic signaling pathways regulated by the secreted protein augurin. Cell Commun. Signal. *21*, 69. https://doi.org/10.1186/S12964-023-01090-8.

56. Chen, R., Liu, Y., Djekidel, M.N., Chen, W., Bhattacherjee, A., Chen, Z., Scolnick,

1127 E., and Zhang, Y. (2022). Cell type-specific mechanism of Setd1a heterozygosity
1128 in schizophrenia pathogenesis. Sci. Adv. *8*, 1077.
1129 https://doi.org/10.1126/sciadv.abm1077.
1130 57. Mukai, J., Cannavò, E., Crabtree, G.W., Sun, Z., Diamantopoulou, A., Thakur, P.,
1131 Chang, C.Y., Cai, Y., Lomvardas, S., Takata, A., et al. (2019). Recapitulation and
1132 Reversal of Schizophrenia-Related Phenotypes in Setd1a-Deficient Mice. Neuron
1133 *104*, 471-487.e12. https://doi.org/10.1016/j.neuron.2019.09.014.
1134 58. MacDonald, M.L., Alhassan, J., Newman, J.T., Richard, M., Gu, H., Kelly, R.M.,
1135 Sampson, A.R., Fish, K.N., Penzes, P., Wills, Z.P., et al. (2017). Selective loss of
1136 smaller spines in Schizophrenia. American Journal of Psychiatry *174*, 586–594.
1137 https://doi.org/10.1176/APPI.AJP.2017.16070814/SUPPL_FILE/APPI.AJP.2017.
1138 16070814.DS001.PDF.
1139 59. Pfeiffer, T., Poll, S., Bancelin, S., Angibaud, J., Inavalli, V.K., Keppler, K., Mittag,
1140 M., Fuhrmann, M., and Nägerl, U.V. (2018). Chronic 2P-STED imaging reveals
1141 high turnover of dendritic spines in the hippocampus in vivo. Elife *7*.
1142 https://doi.org/10.7554/eLife.34700.
1143 60. Attardo, A., Fitzgerald, J.E., and Schnitzer, M.J. (2015). Impermanence of
1144 dendritic spines in live adult CA1 hippocampus. Nature *523*, 592–596.
1145 https://doi.org/10.1038/nature14467.
1146 61. Moriguchi, T., Takeda, S., Iwashita, S., Enomoto, K., Sawamura, T., Koshimizu, U.,
1147 and Kondo, T. (2018). Ecrg4 peptide is the ligand of multiple scavenger receptors.
1148 Sci. Rep. *8*. https://doi.org/10.1038/S41598-018-22440-4.
1149 62. Okabe, S., Kim, H.D., Miwa, A., Kuriu, T., and Okado, H. (1999). Continual
1150 remodeling of postsynaptic density and its regulation by synaptic activity. Nat.
1151 Neurosci. *2*, 804–811. https://doi.org/10.1038/12175.
1152 63. Shin, E., Kashiwagi, Y., Kuriu, T., Iwasaki, H., Tanaka, T., Koizumi, H., Gleeson,
1153 J.G., and Okabe, S. (2013). Doublecortin-like kinase enhances dendritic
1154 remodelling and negatively regulates synapse maturation. Nat. Commun. *4*, 1440.
1155 https://doi.org/10.1038/ncomms2443.
1156 64. Ooe, N., Saito, K., Mikami, N., Nakatuka, I., and Kaneko, H. (2004). Identification
1157 of a novel basic helix-loop-helix-PAS factor, NXF, reveals a Sim2 competitive,
1158 positive regulatory role in dendritic-cytoskeleton modulator drebrin gene
1159 expression. Mol. Cell. Biol. *24*, 608–616. https://doi.org/10.1128/MCB.24.2.608-
1160 616.2004.
1161 65. Ball, G., Demmerle, J., Kaufmann, R., Davis, I., Dobbie, I.M., and Schermelleh, L.
1162 (2015). SIMcheck: a toolbox for successful super-resolution structured illumination

1163 microscopy. Sci. Rep. *5*, 15915. https://doi.org/10.1038/srep15915.
1164 66. Love, M.I., Huber, W., and Anders, S. (2014). Moderated estimation of fold change
1165 and dispersion for RNA-seq data with DESeq2. Genome Biol. *15*.
1166 https://doi.org/10.1186/S13059-014-0550-8.
1167

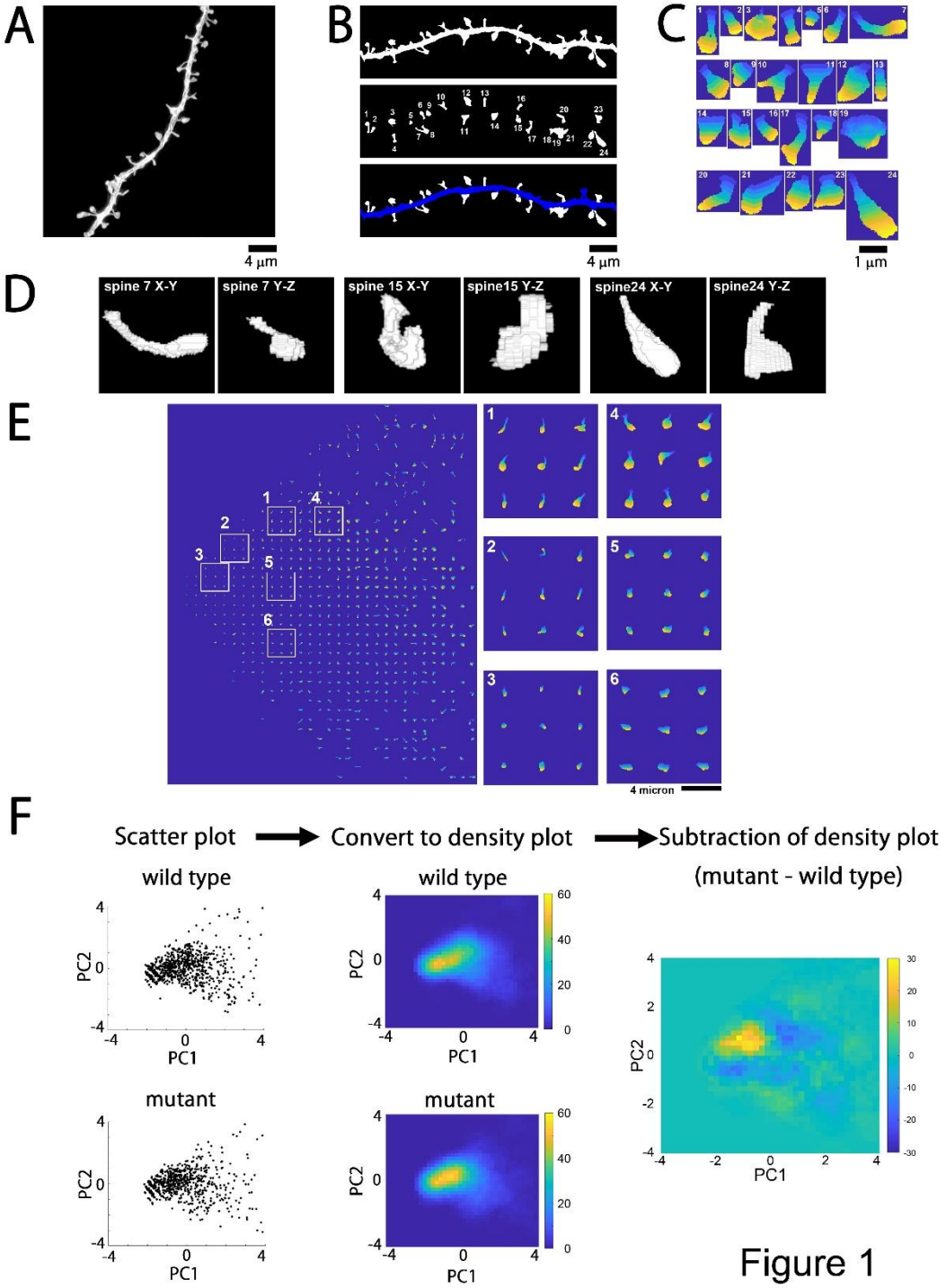
A
B
C
4 µm
4 µm
1 µm
D
spine 7 X-Y
spine 7 Y-Z
spine 15 X-Y
spine15 Y-Z
spine24 X-Y
spine24 Y-Z
E
4 micron
F
Scatter plot
Convert to density plot
Subtraction of density plot
(mutant - wild type)
wild type
mutant
PC1
PC2

Figure 1

1170 **Figure 1**

1171 SIM imaging of dendritic spines, automated measurements of spine morphology, and
1172 generation of subtracted spine density plots for population-level analysis. (A) Original
1173 SIM image of a dendritic shaft stained with lipophilic membrane dye DiI. (B) Binarized
1174 image of the same dendrite (top) and segmented spines numbered from 1 to 24
1175 (middle). The bottom image shows segmented spines (white) and the dendritic shaft
1176 (blue). (C) Enlarged images of the individual spines shown in (B). The pseudocolor
1177 images indicating the relative positions of the spine segments from the base (blue) to
1178 the tip (yellow). (D) 3D views of three spines (No. 7, 15, and 24) viewed from different
1179 angles. (E) Principal component analysis (PCA)-based dimensional reduction of spine
1180 characteristics plotted in the plane of principal components (PC)1 and PC2. (F)
1181 Process of generating a subtracted density plot. The scatter plot of spine distribution in
1182 the PC1–PC2 plane based on morphological parameters was converted into a density
1183 plot for each culture source (genotype or treatment group), and the corresponding plots
1184 were subtracted to reveal differences in spine morphology at the population level. Bars,
1185 4 μm for A, B, and E, 1 μm for C.
1186

1187

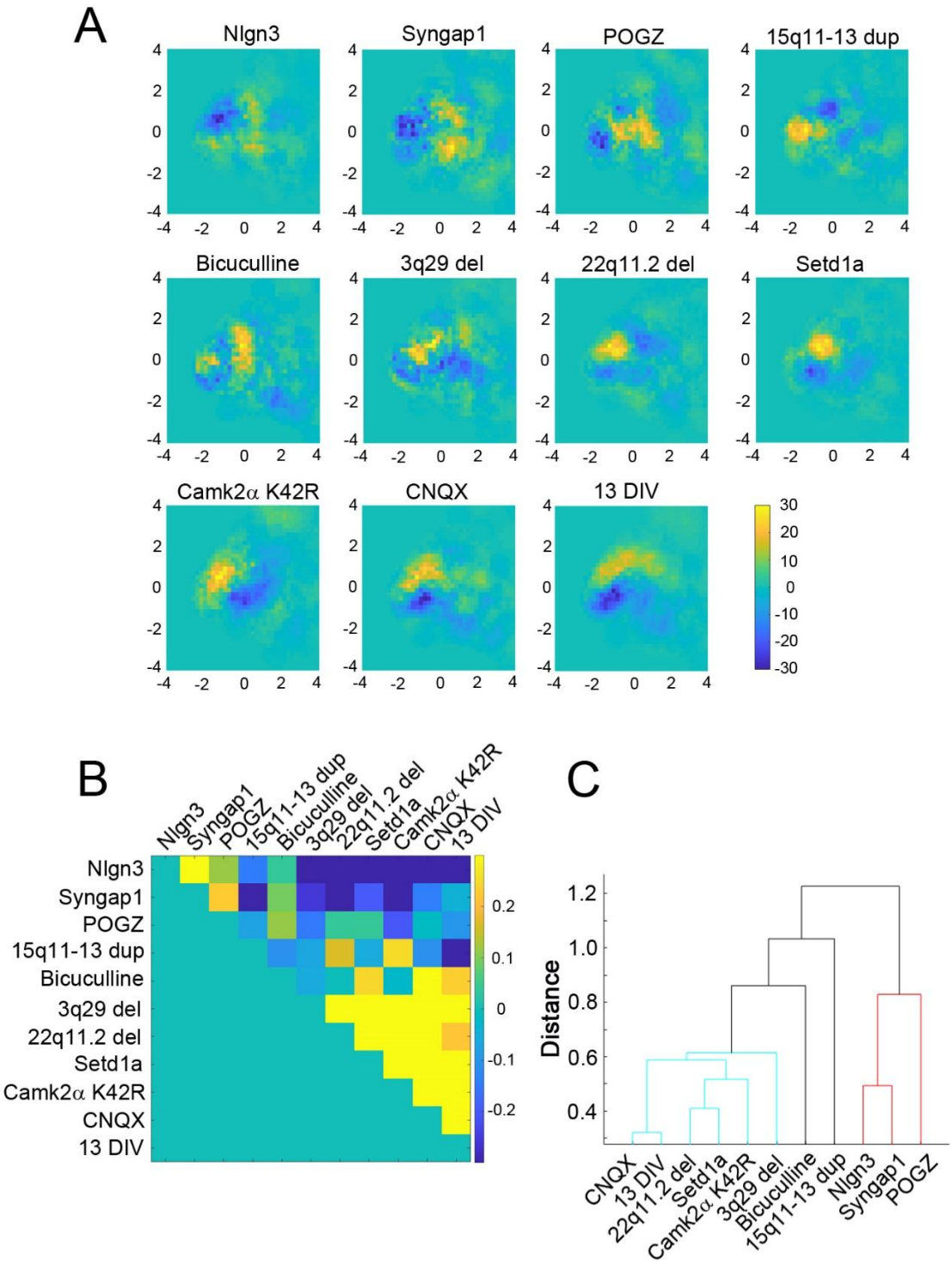
A
Nlgn3
Syngap1
POGZ
15q11-13 dup
Bicuculline
3q29 del
22q11.2 del
Setd1a
Camk2α K42R
CNQX
13 DIV
B
C
Distance
Figure 2

1188

1189

1190 **Figure 2**

1191 Spine population profiles for each model and corresponding control mouse line
1192 presented as subtracted density plots. (A) The subtracted density plots for eight
1193 disease mouse models (Nlgn3$^{R451C/(y\ or\ R451C)}$, Syngap1$^{+/-}$, POGZ$^{Q1038R/+}$, 15q11-13$^{dup/+}$,
1194 3q29$^{del/+}$, 22q11.2$^{del/+}$, Setd1a$^{+/-}$, and CaMKIIα$^{K42R/K42R}$) and three different culture
1195 conditions (immature culture at 13 DIV, AMPA glutamate receptor blocker CNQX
1196 treatment, and $GABA_A$ receptor blocker bicuculine treatment). The areas with a higher
1197 density of spines from mutant disease model mice are shown in yellow, and the areas
1198 with reduced density are shown in blue. The total number of spines (first number, n)
1199 analyzed from control and mutant mouse neurons and the corresponding number of
1200 dendrites (number in parentheses) are as follows: Nlgn3$^{R451C/(y\ or\ R451C)}$; n = 1,134 (58)
1201 and 1,204 (59), Syngap1$^{+/-}$; n = 991 (65) and 1,371 (83), POGZ$^{Q1038R/+}$; n = 1,341 (72)
1202 and 1,271 (72), 15q11-13$^{dup/+}$; n = 1, 208 (68) and 1,099 (63), 3q29$^{del/+}$; n = 1,429 (66)
1203 and 1,408 (66), 22q11.2$^{del/+}$; n = 1,143 (66) and 914 (63), Setd1a$^{+/-}$; n = 1,381 (71) and
1204 1,405 (71), CaMKIIα$^{K42R/K42R}$; n = 880 (58) and 763 (54). All data are from three
1205 independent culture preparations. (B) Matrix of the 2D cross-correlations among
1206 subtracted density plots. In the lower right area, a spine group showing similar
1207 morphological changes can be identified. This group corresponded to the mouse
1208 models of schizophrenia. (C) Unbiased clustering of spine samples showing two
1209 distinct groups corresponding to schizophrenia (cyan) and ASD (red).

1210

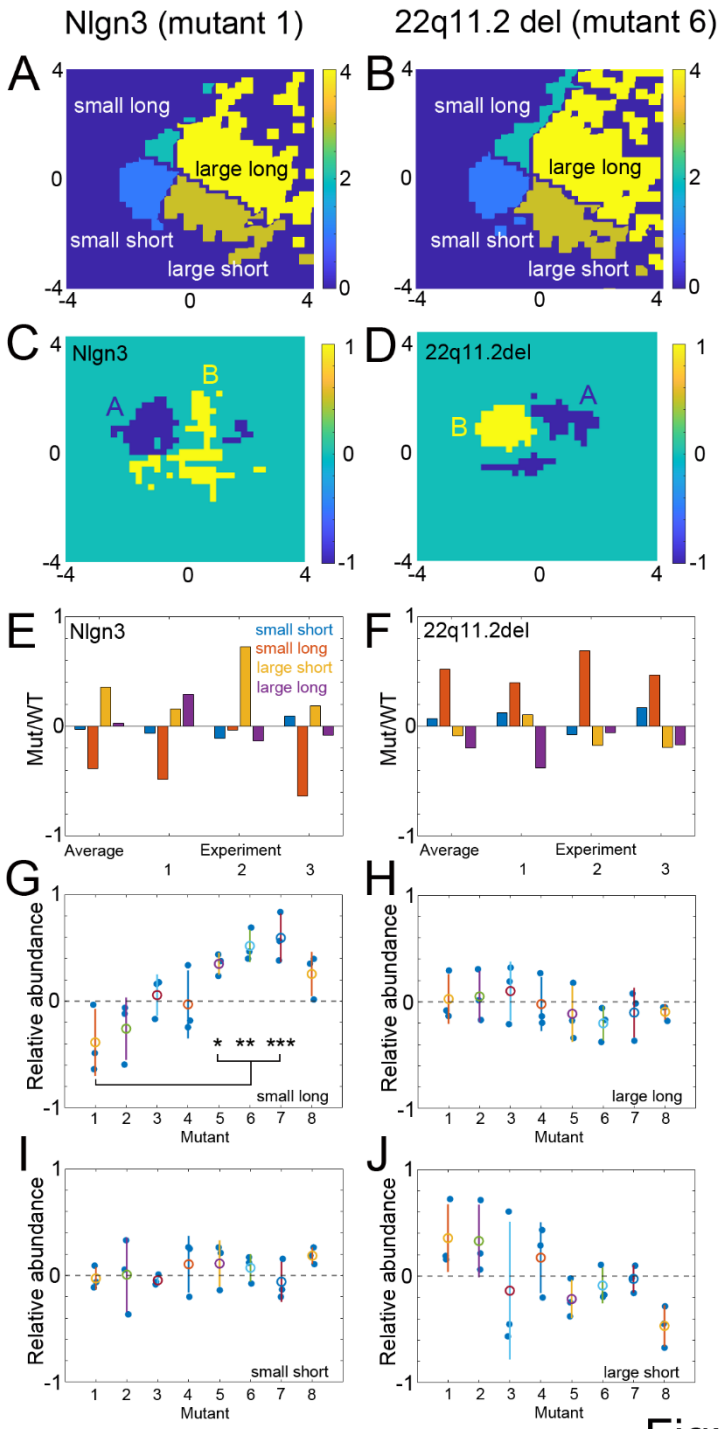

Figure 3

1211
1212

1213 **Figure 3**

1214 Distinct morphological properties of spines in cultured neurons derived from
1215 schizophrenia model mice compared with ASD model mice.

1216 (A, C, and E) Relative enrichment of four different subgroups of spines in Nlgn3$^{R451C/(y\ or}$
1217 $^{R451C)}$ neurons compared with wild-type neurons. In the projection plane of PC1 and
1218 PC2, four areas with distinct structural properties, namely (1) small and short, (2) small
1219 and long, (3) large and short, and (4) large and long, were defined (A). The map of
1220 areas with large differences (> 3 × SD) between control and mutant mice in spine
1221 number per area in the feature space (C) indicates that the area enriched with wild-type
1222 spines (area B, yellow region) overlaps with the area of large spines. The area
1223 enriched with the mutant spines overlaps with the area of small spines (area A, blue
1224 region). The relative enrichment of mutant spines was summarized in (E).

1225 (B, D, and F) Similar analysis of mutant spine enrichment in 22q11.2$^{del/+}$ neurons. The
1226 map of spine distribution with four different properties (B), the map of areas enriched
1227 with wild-type or mutant spines (D), and the graph of relative enrichment of mutant
1228 spines (F) show that the mutant neurons were enriched with small and long spines.

1229 (G-J) Relative abundance of the four subgroups of spines in 8 mutant mouse models
1230 (1: Nlgn3$^{R451C/(y\ or\ R451C)}$, 2: Syngap1$^{+/-}$, 3: POGZ$^{Q1038R/+}$, 4: 15q11-13$^{dup/+}$, 5: 3q29$^{del/+}$, 6:
1231 22q11.2$^{del/+}$, 7: Setd1a$^{+/-}$, 8: CaMKIIα$^{K42R/K42R}$). Three independent culture experiments
1232 with paired wild-type and mutant samples were performed. Group comparisons were
1233 performed using one-way ANOVA followed by Tukey's post hoc test. (* $p < 0.05$, ** $p <$
1234 0.01, *** $p < 0.005$).

1235

1236

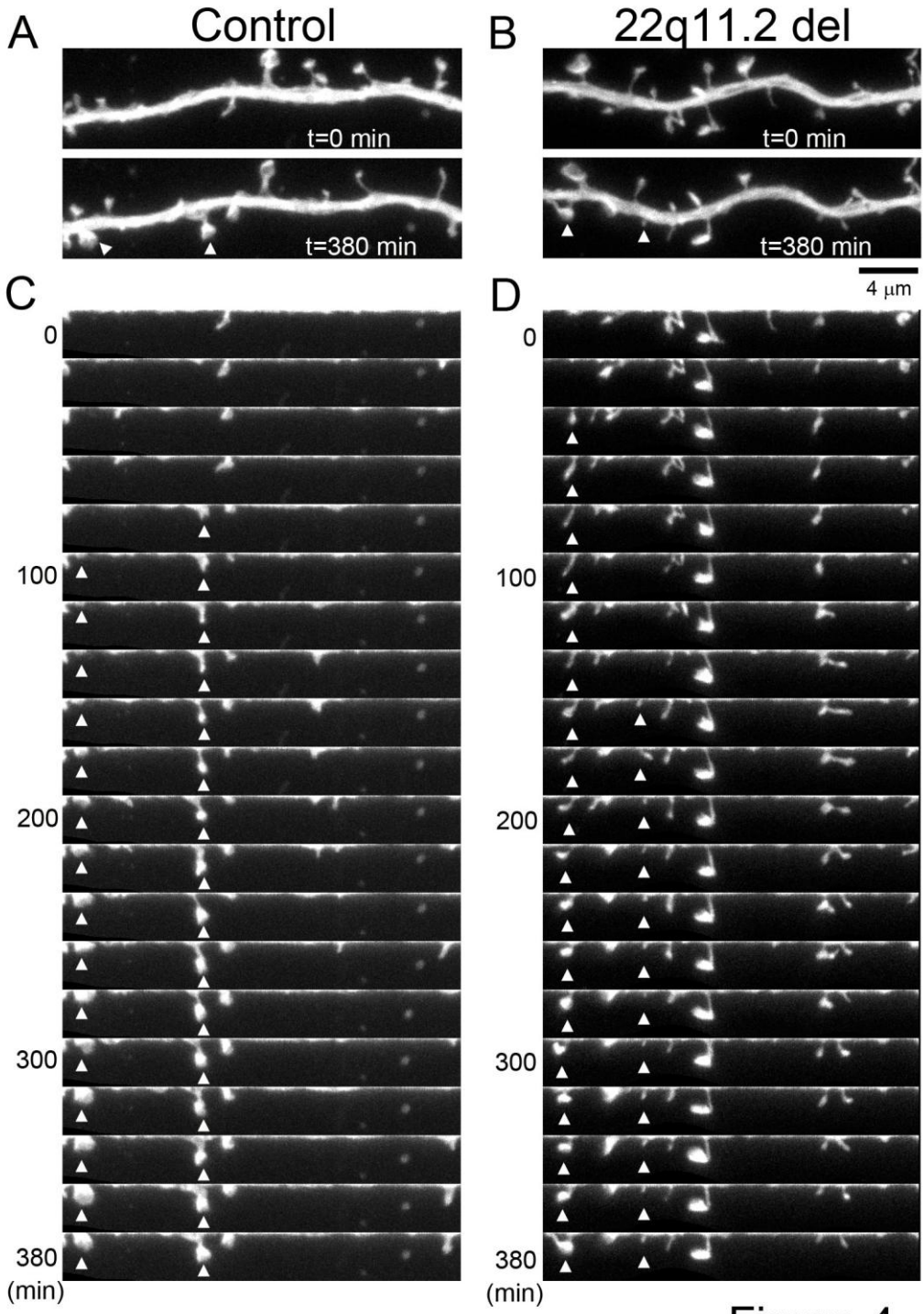

Figure 4

1237

1238

1239

1240

1241 **Figure 4**

1242 Time-lapse imaging of neurons derived from 22q11.2$^{del/+}$ mice and corresponding
1243 control mice. (A and B) Images of dendritic segments from control neurons (A) and
1244 22q11.2$^{del/+}$ neurons (B) at two different time points. (C and D) Montages of time-lapse
1245 images from control neurons (C) and 22q11.2$^{del/+}$ neurons (D). The curved dendrites
1246 were straightened, revealing newly formed spines (arrowheads) as fluorescent objects
1247 appearing at the edge of the dendritic shafts. Bar, 4 μm.

1248

1249

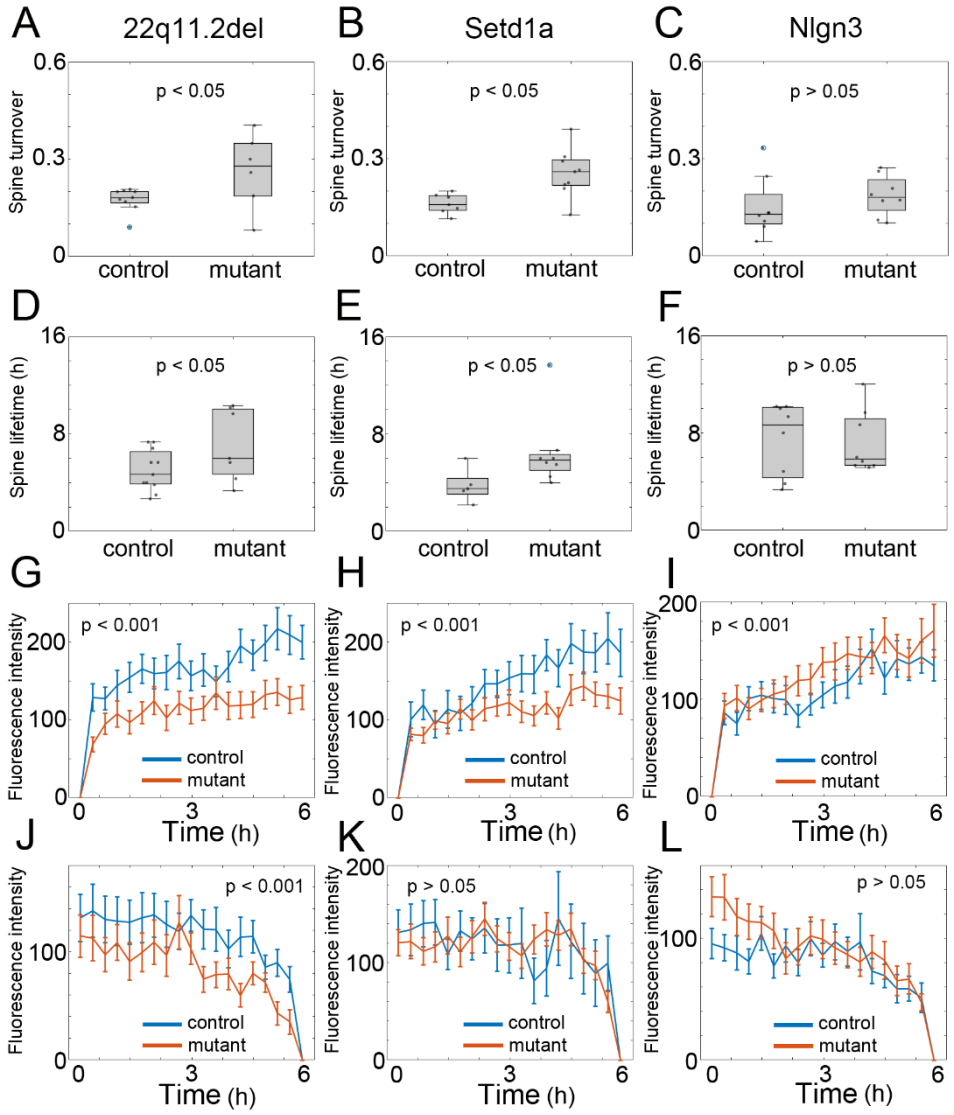

Figure 5

1250

1251

1252

1253 **Figure 5**

1254 Turnover rate, lifetime, and growth/shrinkage profiles of dendritic spines in cultured
1255 neurons derived from 22q11.2$^{del/+}$, Setd1a$^{+/-}$, and Nlgn3$^{R451C/(y\ or\ R451C)}$ mice, as well as
1256 the corresponding controls. (A-C) Spine turnover rates in the three mutant mouse
1257 models compared to the controls. Spine turnover rates were analyzed using a linear
1258 mixed-effects model with genotype as a fixed effect and plate, cell, and dendrite as
1259 nested random effects, showing a significant effect of genotype only in 22q11.2$^{del/+}$ and
1260 Setd1a$^{+/-}$ mice (n = 16 dendrites/9 cells/5 plates in control and 11 dendrites/6 cells/4
1261 plates in 22q11.2$^{del/+}$, n = 10 dendrites/7 cells/4 plates in control and n = 14 dendrites/9
1262 cells/6 plates in Setd1a$^{+/-}$, n = 8 dendrites/8 cells/3 plates in control and n = 8
1263 dendrites/8 cells/3 plates in Nlgn3$^{R451C/(y\ or\ R451C)}$). (D-F) Lifetimes of transient spines for
1264 the three mutant mouse models compared with corresponding controls. Spine lifetime
1265 was analyzed using a linear mixed-effects model accounting for the hierarchical
1266 structure of the data (spines nested within dendrites, cells, and culture plates). The
1267 analysis revealed a significant effect of genotype only in 22q11.2$^{del/+}$ and Setd1a$^{+/-}$
1268 neurons (n = 186 spines/11 dendrites/7 cells/5 plates in control and n = 166 spines/7
1269 dendrites/4 cells/4 plates in 22q11.2$^{del/+}$, n = 82 spines/5 dendrites/5 cells/4 plates in
1270 control and n = 202 spines/8 dendrites/8 cells/5 plates in Setd1a$^{+/-}$, n = 98 spines/8
1271 dendrites/8 cells/3 plates in control and n = 125 spines/8 dendrites/8 cells/3 platess in
1272 Nlgn3$^{R451C/(y\ or\ R451C)}$). (G-I) Temporal patterns of spine growth (n = 60 spines/11
1273 neurons/7 cells/5 plates in control and n = 50 spines/7 dendrites/4 cells/4 plates in
1274 22q11.2$^{del/+}$, n = 25 spines/5 dendrites/5 cells/4 plates in control and n = 65 spines /8
1275 dendrites/8 cells/5 plates in Setd1a$^{+/-}$, n = 43 spines/8 dendrites/8 cells/3 plates in
1276 control and n = 41 spines/7 dendrites/7 cells/2 plates in Nlgn3$^{R451C/(y\ or\ R451C)}$). Spine

1277 volume trajectories were analyzed using linear mixed-effects models incorporating
1278 nested random effects (spine within dendrite within cell within culture plate) to account
1279 for the hierarchical structure of the data. Newly formed spines in both 22q11.2$^{del/+}$ and
1280 Setd1a$^{+/-}$ neurons were significantly smaller than those in wild-type neurons. In
1281 contrast, newly formed spines in Nlgn3$^{R451C/(y\ or\ R451C)}$ neurons were significantly larger
1282 than those in wild-type neurons. (J-L) Temporal patterns of spine shrinkage (n = 39
1283 spines/10 dendrites/6 cells/5 plates in control and n = 37 spines/7 dendrites/4 cells/4
1284 plates in 22q11.2$^{del/+}$, n = 15 spines/5 dendrites/5 cells/4 plates in control and n = 55
1285 spines/8 dendrites/8 cells/5 plates in Setd1a$^{+/-}$, n = 28 spines/8 dendrites/8 cells/3
1286 plates in control and n = 35 spines/8 dendrites/8 cells/3 plates Nlgn3$^{R451C/(y\ or\ R451C)}$
1287 neurons). Spine volume trajectories were analyzed using linear mixed-effects models
1288 as in (G-I). In the 22q11.2$^{del/+}$ neurons, spines undergoing elimination were significantly
1289 smaller than those in wild-type neurons. This effect was not detected in Setd1a$^{+/-}$ and
1290 Nlgn3$^{R451C/(y\ or\ R451C)}$ neurons.
1291

1292

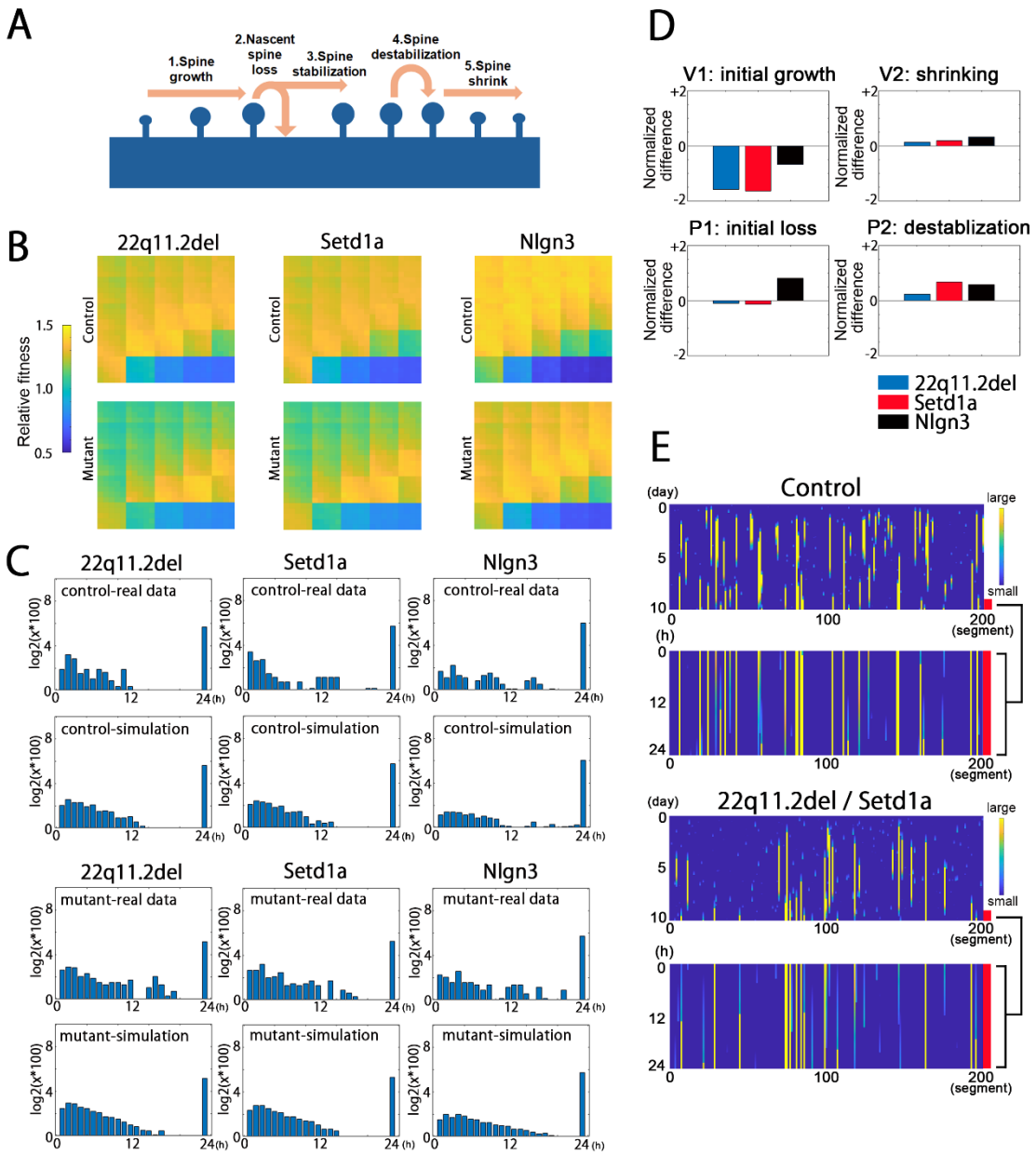

Figure 6

1293

1294

1295

1296

1297

1298 **Figure 6**

1299 Simulations of long-term spine turnover. (A) The model of spine dynamics. Five
1300 successive phases of spine state transitions were defined. Phase 1: newly formed
1301 spines grow at speed V1. Phase 2: nascent spines are eliminated with probability P1.
1302 Phase 3: nascent spines are stabilized when volume reaches an upper threshold.
1303 Phase 4: stable spines are destabilized with probability P2. Phase 5: spines shrinking
1304 at a rate V2 are lost after reaching a lower threshold. (B) Pseudocolor maps of 625
1305 different combinations of these parameters to identify those best fitting the
1306 experimental data. The color-coded values indicate the fitness of the simulation results
1307 to both the spine lifetime distribution profile and the turnover rate. (C) Frequency
1308 histograms of spine lifetimes for the three mouse models and controls (experimental
1309 data), and the results of simulations. The bin with a lifetime of 24 h corresponds to the
1310 spines that persisted throughout the imaging period. (D) Differences in V1, V2, P1, and
1311 P2 between mutant mice and controls, expressed as differences in the four parameters
1312 normalized by the control condition values. (E) Plots of individual spine turnover
1313 simulated using parameters that best fit the experimental data from control and
1314 schizophrenia-associated mouse models. The upper plots show the progression of
1315 spine formation along 200 dendritic segments (50 μm) over 10 days. The lower plots
1316 show the enlargement of the last 24 h of spine turnover. Color indicates spine size.
1317

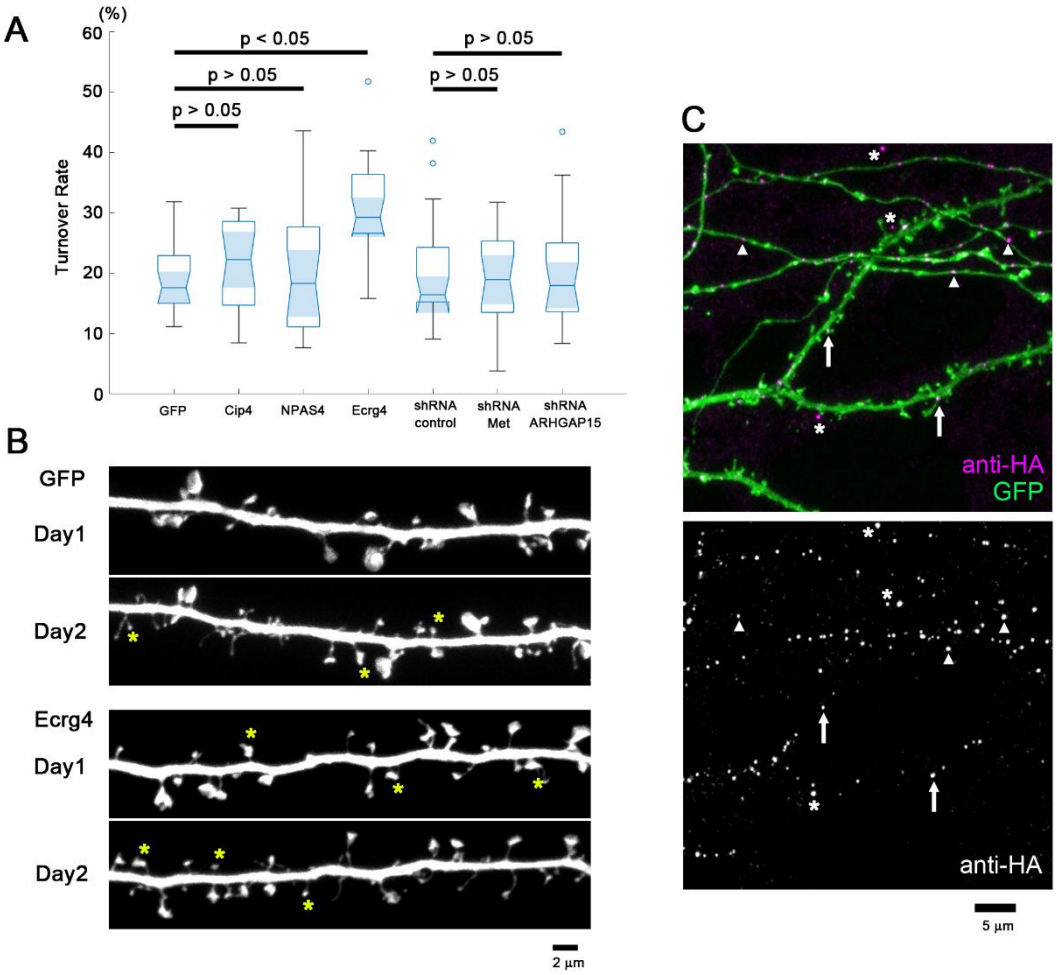
A
(%)
Turnover Rate
p < 0.05
p > 0.05
p > 0.05
p > 0.05
p > 0.05
GFP
Cip4
NPAS4
Ecrg4
shRNA control
shRNA Met
shRNA ARHGAP15
B
GFP
Day1
Day2
Ecrg4
Day1
Day2
2 µm
C
anti-HA
GFP
anti-HA
5 µm

Figure 7

1328 **Figure 7**

1329 Manipulation of candidate gene expression in wild-type hippocampal neurons and its
1330 effects on spine turnover. (A) Turnover rates of dendritic spines in neurons transfected
1331 with an overexpression plasmid encoding Cip4, Npas4, or Ecrg4, or a plasmid
1332 encoding an shRNA targeting Met or Arhgap15, together with a GFP expression
1333 plasmid. Spine turnover rates were calculated from the images of GFP-expressing
1334 dendrites taken at an interval of 24 h. Among the five DEGs, only the upregulation of
1335 Ecrg4 selectively increased the spine turnover rate. Linear mixed-effects modeling with
1336 experiment as a random factor revealed a significant effect of overexpression treatment
1337 ($F(3,8)=4.59$, $p=0.038$), driven by Ecrg4 ($p=0.013$), whereas shRNA manipulations
1338 showed no significant effect ($F(2,6)=0.29$, $p=0.76$). (results from n = 22 dendrites/11
1339 neurons/3 culture plates derived from independent primary culture for all conditions
1340 except the Met shRNA groups, where n = 21 dendrites from 11 neurons were included
1341 in the analysis). (B) Fluorescence images of dendritic segments expressing GFP or
1342 GFP plus Ecrg4 on days 1 and 2. Newly formed spines are marked by asterisks. Bar, 2
1343 μm. (C) Images of dendrites and axons expressing HA-tagged Ecrg4 together with
1344 GFP. Anti-HA immunocytochemistry revealed the presence of immunopositive puncta
1345 both in the dendrites (arrows) and axons (arrowheads). Some clusters could be
1346 detected in the extracellular space (asterisks). The upper image is the overlay of the
1347 anti-HA signal (magenta) and GFP (green). The lower image shows the distribution of
1348 the anti-HA signals. Bar, 5 μm.
1349

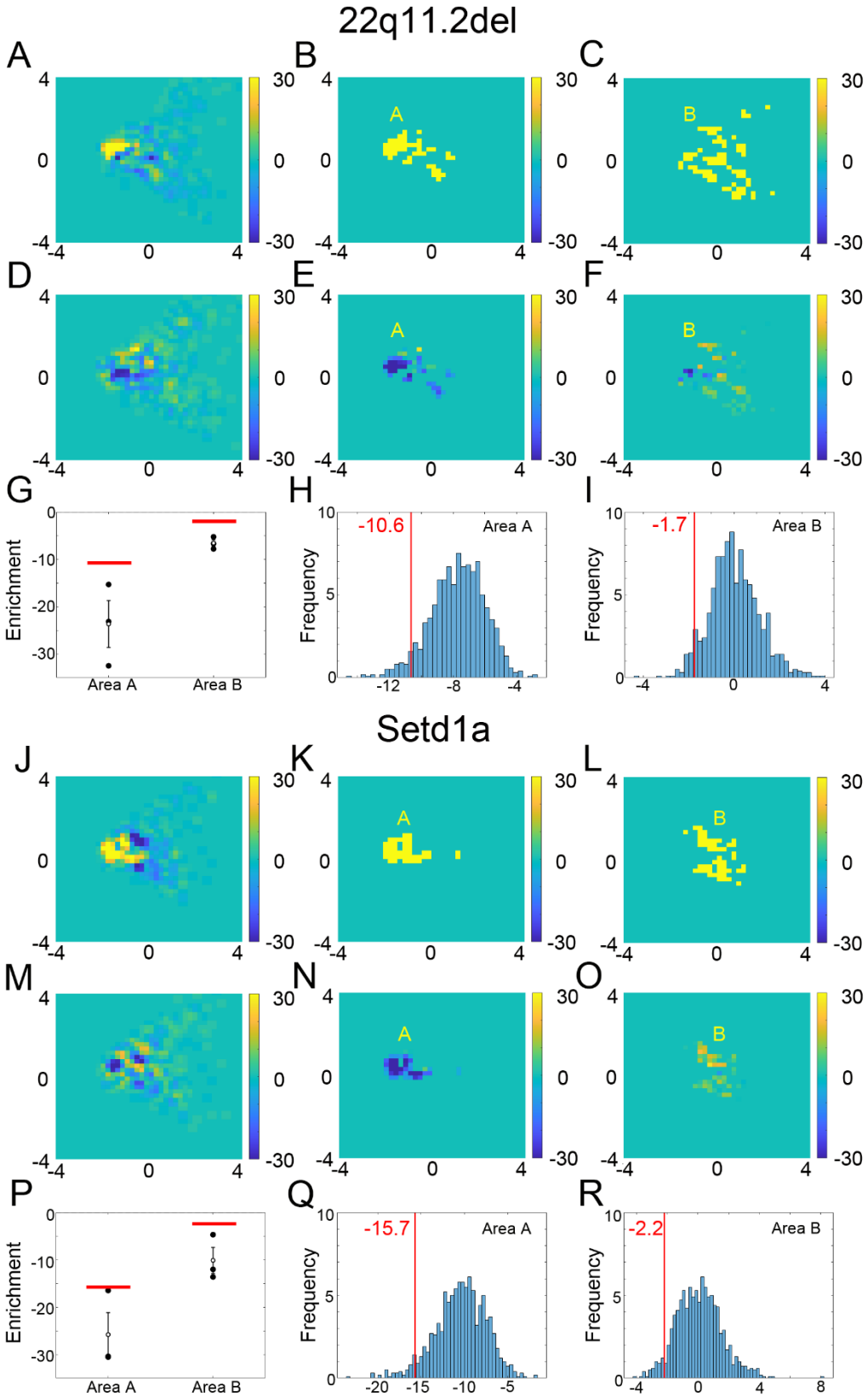

Figure 8

1350

1351 **Figure 8**

1352 Altered spine population profiles after suppression of Ecrg4 expression in neurons
1353 derived from two schizophrenia-associated mouse models: the 22q11.2$^{del/+}$ mouse
1354 model (A-I) and Setd1a$^{+/-}$ mouse model (J-R). (A and J) Density plot obtained by
1355 subtracting wild-type spines from mutant spines. Both wild-type and mutant neurons
1356 expressed control shRNA. (B and K) Area enriched with the mutant spines under the
1357 control shRNA condition. (C and L) Area depleted of the mutant spines under the
1358 control shRNA condition. (D and M) Density plot obtained by subtraction of the wild-
1359 type spines under control shRNA from the mutant spines under Ecrg4 shRNA. This
1360 subtraction illustrates the normalizing effect of Ecrg4 shRNA. (E and N) Reduction of
1361 mutant spines in area A by Ecrg4 shRNA. The density plot, obtained by subtracting the
1362 mutant spines under control shRNA from those under Ecrg4 shRNA, shows the extent
1363 of normalization by Ecrg4 shRNA. (F and O) The increase of mutant spines in area B
1364 by Ecrg4 shRNA using the same subtraction method. (G and P) The extent of rescue
1365 by Ecrg4 shRNA in Area A and B for three independent culture experiments using
1366 either 22q11.2$^{del/+}$ or Setd1a$^{+/-}$ mouse models. The red lines show the values
1367 corresponding to statistical significance ($p = 0.05$), estimated from permutation
1368 analyses shown in (H, I, Q, and R). (H and Q) Permutation analysis for Area A to
1369 estimate the 95th percentile of the shuffled data. (I and R) Permutation analysis for
1370 Area B.

1371

Supplementary Figures and Legends

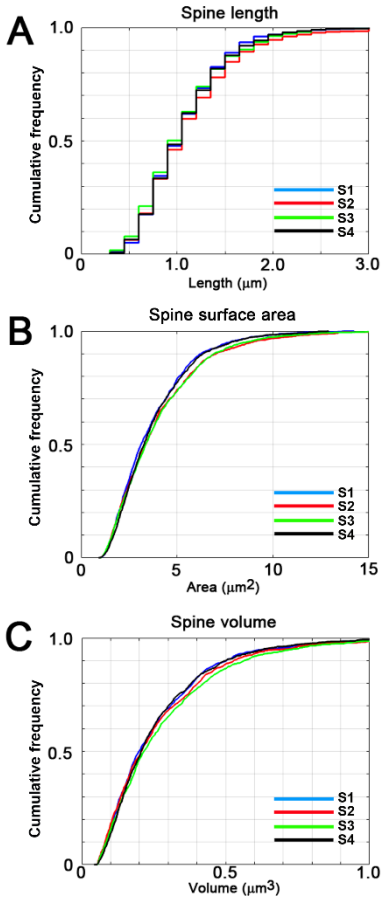

Supplementary Figure 1

Supplementary Figure 1

Cumulative frequency plots of spine length, surface area, and volume measured in four independent experiments performed > 2 months apart. The cumulative frequency distributions of spine length (A), spine surface area (B), and spine volume (C) were obtained from wild-type data acquired by SIM imaging across four mouse models: Nlgn3$^{R451C/(y\ or\ R451C)}$ (S1), Syngap1$^{+/-}$ (S2), POGZ$^{Q1038R/+}$ (S3), and 15q11-13$^{dup/+}$ (S4). The Kolmogorov–Smirnov test detected significant differences in only three of 18 possible pairwise comparisons: surface area of (S1) vs. (S3) ($p = 0.017$), volume of (S1) vs. (S3) ($p = 0.032$), and volume of (S3) vs. (S4) ($p = 0.038$).

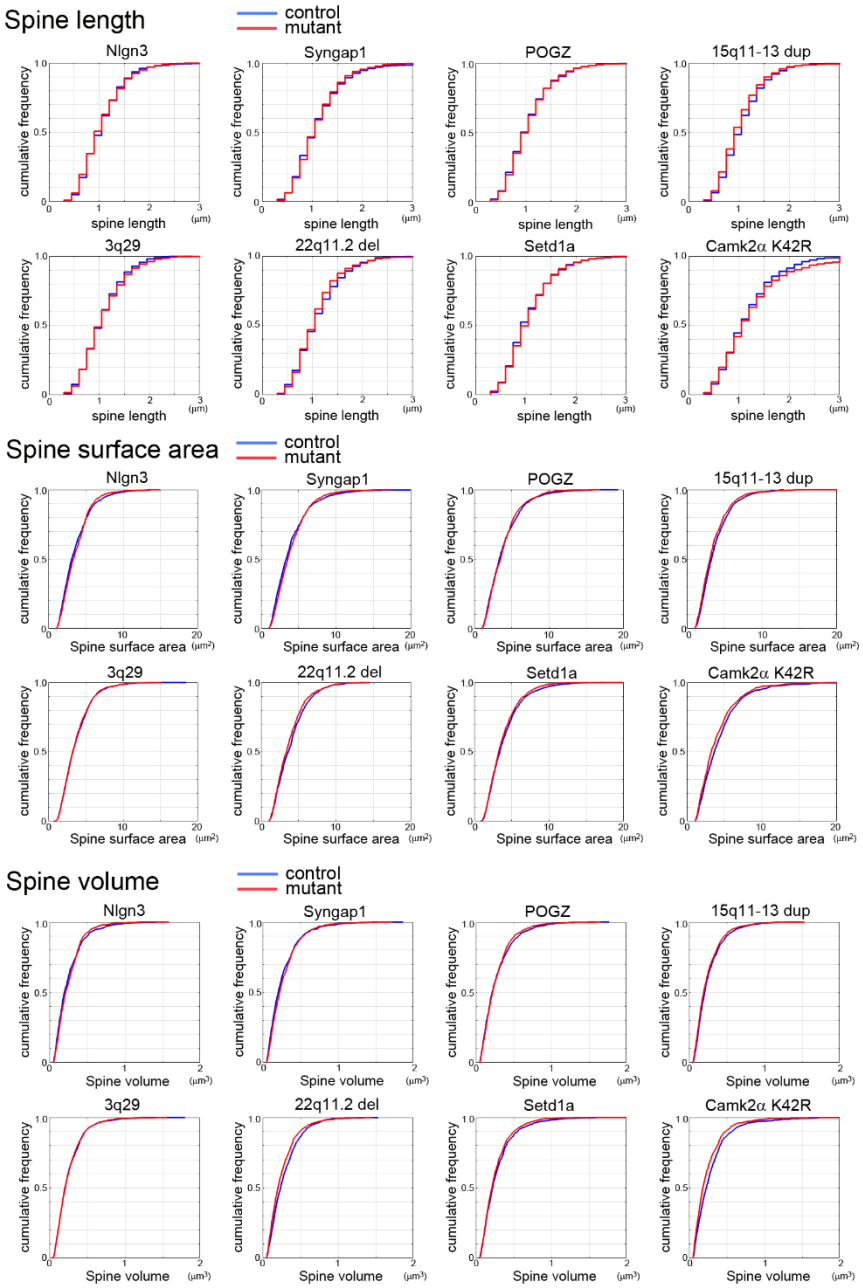

Supplementary Figure 2

Supplementary Figure 2

Cumulative frequency plots of spine length, surface area, and volume for the eight mouse mutants: Nlgn3$^{R451C/(y\ or\ R451C)}$, Syngap1$^{+/-}$, POGZ$^{Q1038R/+}$, 15q11-13$^{dup/+}$, 3q29$^{del/+}$, 22q11.2$^{del/+}$, Setd1a$^{+/-}$, and CaMKIIα$^{K42R/K42R}$.

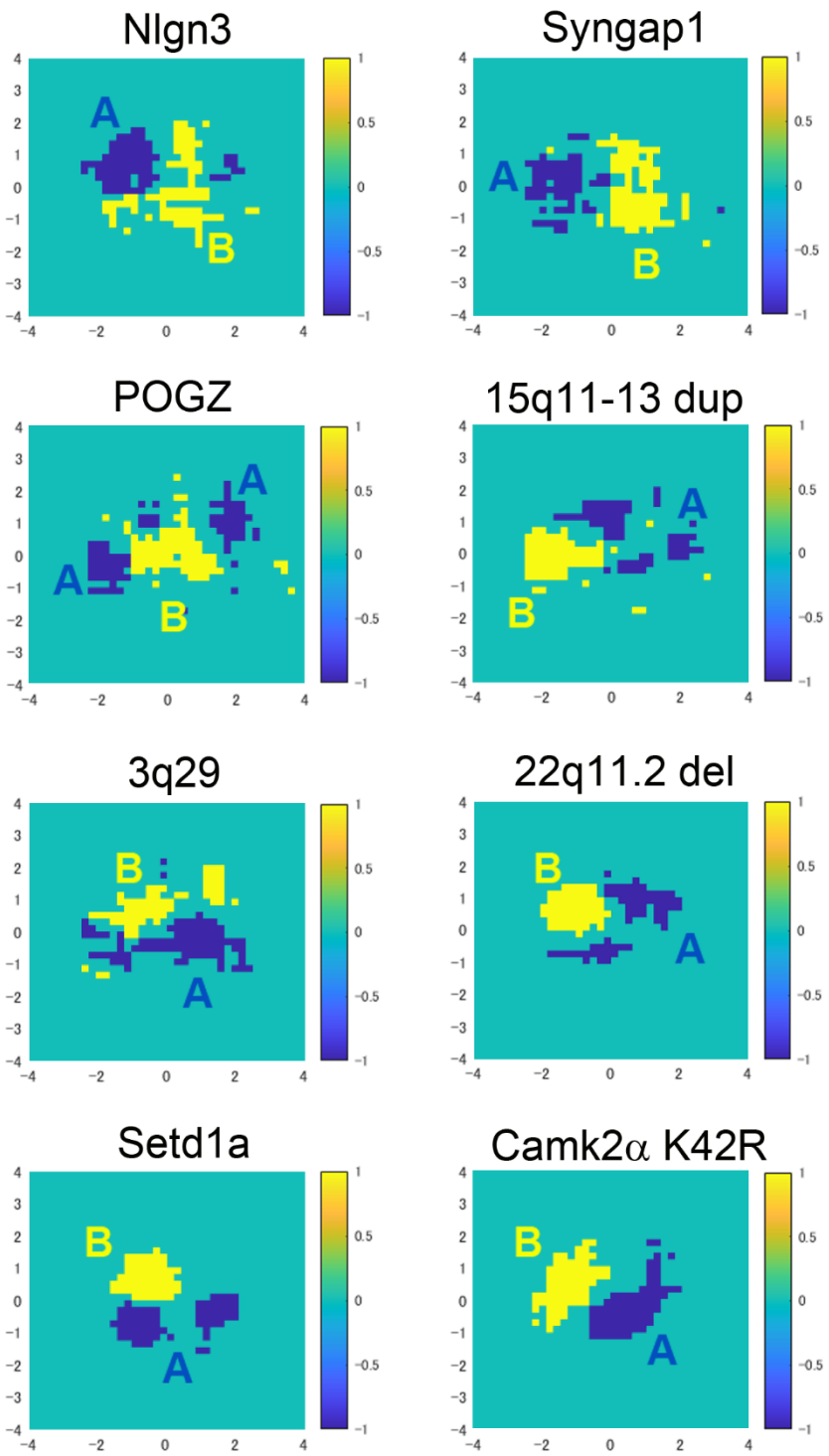

A: wild type > mutant
B: mutant > wild type

Supplementary Figure 3

1391 **Supplementary Figure 3**

1392 Areas where control (A: blue) or mutant (B: yellow) spines show a higher density within
1393 the feature space of the PC1-PC2 plane. The plots for all 8 mouse models are
1394 presented. The differences in population-level spine properties between ASD- and
1395 schizophrenia-associated mouse models were preserved within two groups. The areas
1396 enriched with mutant spines in Nlgn3$^{R451C/(y\ or\ R451C)}$, Syngap1$^{+/-,}$ and POGZ$^{Q1038R/+}$
1397 models were on the right side of the plot, suggesting the abundance of large spines in
1398 this group. In contrast, the areas enriched with mutant spines in 3q29$^{del/+}$, 22q11.2$^{del/+}$,
1399 Setd1a$^{+/-}$, and CaMKIIα$^{K42R/K42R}$ models were positioned on the left side of the plot,
1400 indicating the abundance of small spines.
1401

1402

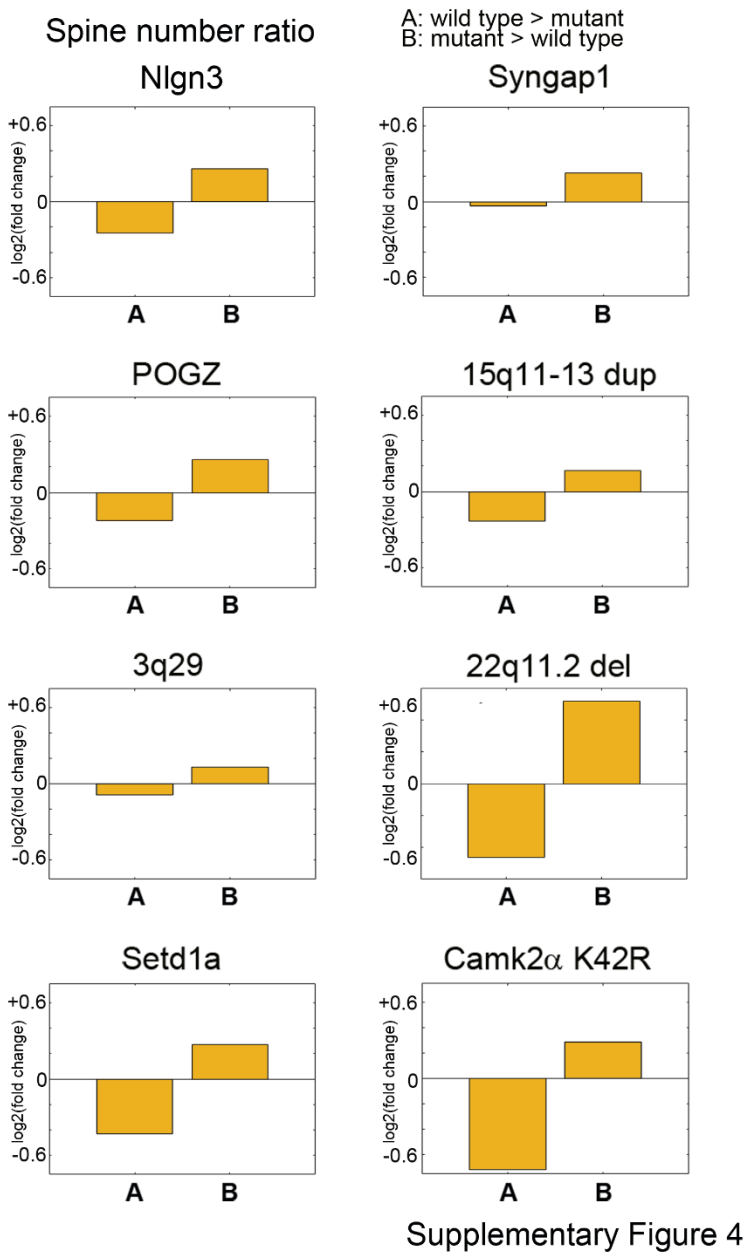

1403

1404

1405 **Supplementary Figure 4**

1406 The relative numbers of spines within areas A and B in the feature space from

1407 Supplementary Figure 3. The densities of mutant spines were higher in area B than in

1408 area A.

1409

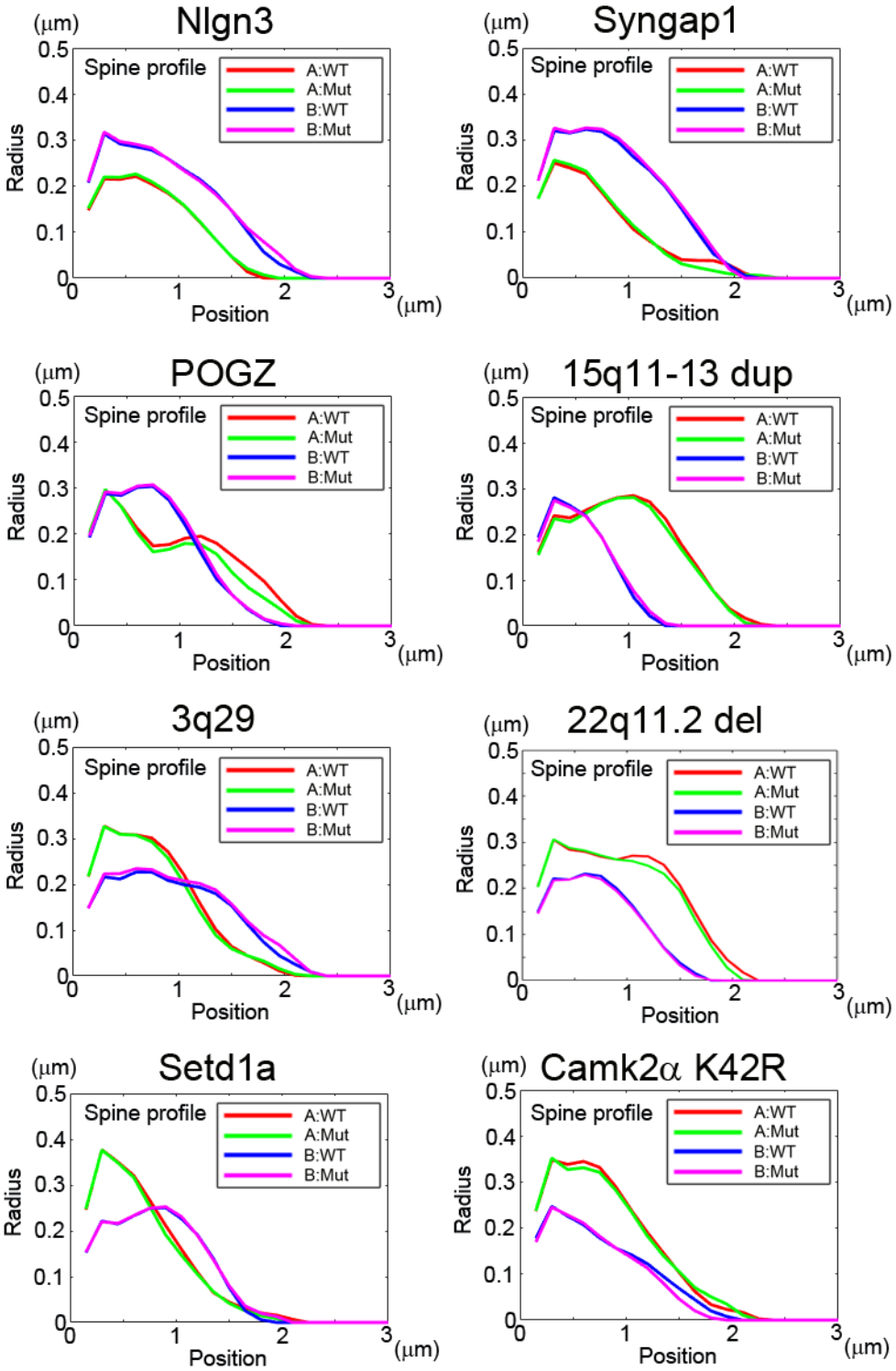

A: wild type > mutant
B: mutant > wild type

Supplementary Figure 5

1410

1411 **Supplementary Figure 5**

1412 Profiles of different spine populations (spines in the control-dominant area A and the
1413 mutant-dominant area B for both wild-type and mutant neurons) were visualized by
1414 plotting the radius along the long axis. The numbers of control and mutant spines
1415 included in the analysis are as follows: Nlgn3$^{R451C/(y\ or\ R451C)}$, n = 775 in area A and n =
1416 513 in area B; Syngap1$^{+/-}$, n = 668 in area A and n = 500 in area B; POGZ$^{Q1038R/+}$, n =
1417 580 in area A and n = 815 in area B; 15q11-13$^{dup/+}$, n = 378 in area A and n = 797 in
1418 area B; 3q29$^{del/+}$, n = 627 in area A and n = 824 in area B; 22q11.2$^{del/+}$, n = 308 in area
1419 A and n = 575 in area B; Setd1a$^{+/-}$, n = 472 in area A and n = 808 in area B;
1420 CaMKIIα$^{K42R/K42R}$, n = 237 in area A and n = 634 in area B.
1421

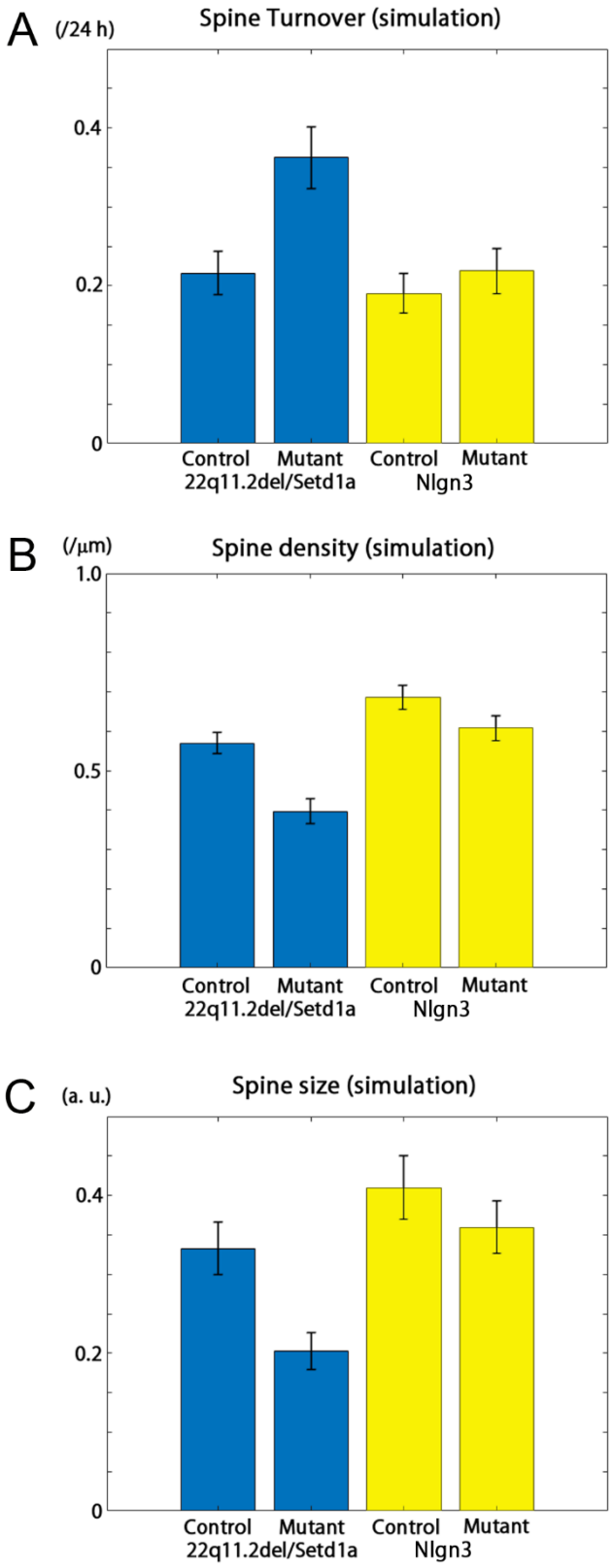

Supplementary Figure 6

1422

Supplementary Figure 6

Spine turnover (A), density (B), and size (C) from simulation data. Simulation parameters were tuned to fit experimental results from control and mutant models. Means and standard deviations are shown.

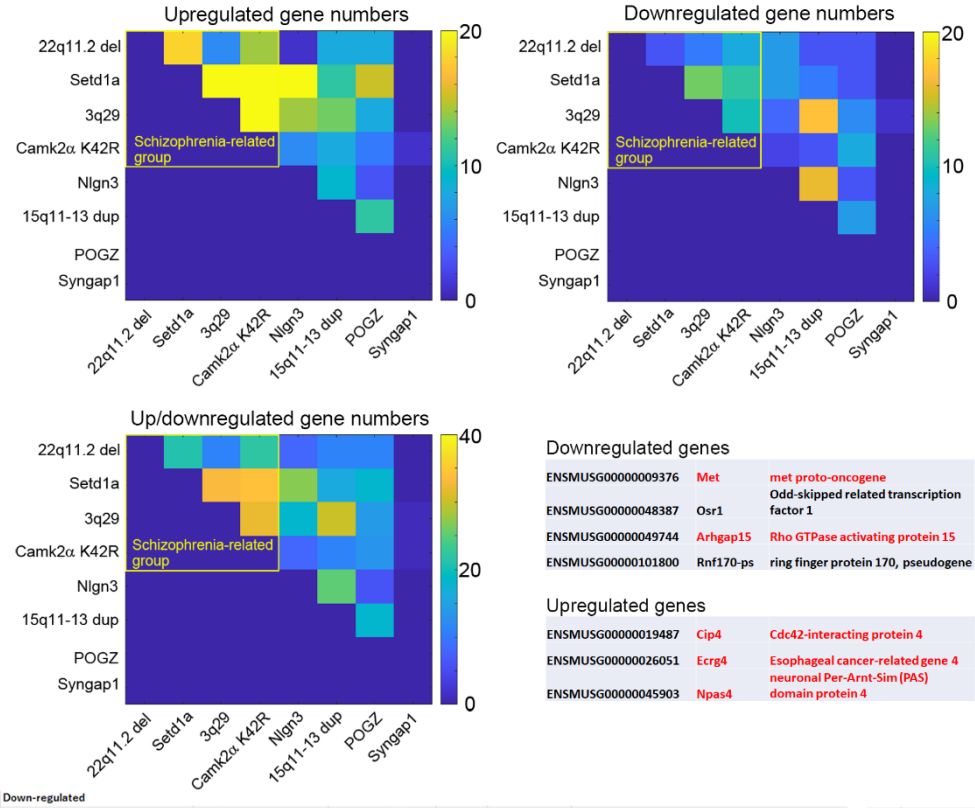

Downregulated genes

ENSMUSG00000009376	Met	met proto-oncogene
ENSMUSG00000048387	Osr1	Odd-skipped related transcription factor 1
ENSMUSG00000049744	Arhgap15	Rho GTPase activating protein 15
ENSMUSG00000101800	Rnf170-ps	ring finger protein 170, pseudogene

Upregulated genes

ENSMUSG00000019487	Cip4	Cdc42-interacting protein 4
ENSMUSG00000026051	Ecrg4	Esophageal cancer-related gene 4
ENSMUSG00000045903	Npas4	neuronal Per-Arnt-Sim (PAS) domain protein 4

Down-regulated

	gene ID	mouse model No		gene name	property
In only mouse models 5-8	ENSMUSG00000009376	123	schizo	Met	met proto-oncogene
In only mouse models 5-8	ENSMUSG00000048387	234	schizo	Osr1	Odd-skipped related transcription factor 1
In only mouse models 5-8	ENSMUSG00000049744	234	schizo	Arhgap15	Rho GTPase activating protein 15
In only mouse models 5-8	ENSMUSG00000101800	234	schizo	Rnf170-ps	ring finger protein 170, pseudogene
In only mouse models 1-4	ENSMUSG00000021125	567	ASD	Arg2	arginase type II
In both 1-4 group and 5-8 group	ENSMUSG00000016493	256	common	Cd46	CD46 antigen, complement regulatory protein
In both 1-4 group and 5-8 group	ENSMUSG00000024176	367	common	Sox8	Transcription factor SOX-8
In both 1-4 group and 5-8 group	ENSMUSG00000032487	157	common	Ptgs2	prostaglandin-endoperoxide synthase 2, COX2
In both 1-4 group and 5-8 group	ENSMUSG00000055093	347	common	Gm8430	ribosomal protein S27A, pseudogene 3
In both 1-4 group and 5-8 group	ENSMUSG00000097585	456	common	E230029C05Rik	lncRNA gene, RIKEN cDNA E230029C05 gene
In both 1-4 group and 5-8 group	ENSMUSG00000118125	356	common	Gm50387	predicted gene, 50387

Up-regulated

	gene ID	mouse model No		gene name	property
In only mouse models 5-8	ENSMUSG00000019487	234	schizo	Trip10	Thyroid Hormone Receptor Interactor 10
In only mouse models 5-8	ENSMUSG00000026051	124	schizo	Ecrg4	Esophageal cancer-related gene 4
In only mouse models 5-8	ENSMUSG00000045903	234	schizo	Npas4	neuronal Per-Arnt-Sim (PAS) domain protein 4
In both 1-4 group and 5-8 group	ENSMUSG00000003545	346	common	Fosb	FBJ osteosarcoma oncogene B
In both 1-4 group and 5-8 group	ENSMUSG00000020218	367	common	Wif1	Wnt inhibitory factor 1
In both 1-4 group and 5-8 group	ENSMUSG00000020473	235	common	Aebp1	Adipocyte Enhancer-binding Protein 1
In both 1-4 group and 5-8 group	ENSMUSG00000021214	267	common	Akr1c18	aldo-keto reductase family 1, member C18
In both 1-4 group and 5-8 group	ENSMUSG00000021250	346	common	Fos	FBJ osteosarcoma oncogene
In both 1-4 group and 5-8 group	ENSMUSG00000026579	345	common	F5	coagulation factor V
In both 1-4 group and 5-8 group	ENSMUSG00000027107	346	common	Chrna1	cholinergic receptor nicotinic alpha 1 subunit
In both 1-4 group and 5-8 group	ENSMUSG00000032232	234	common	Cgnl1	cingulin-like 1
In both 1-4 group and 5-8 group	ENSMUSG00000032334	345	common	Loxl1	lysyl oxidase-like 1
In both 1-4 group and 5-8 group	ENSMUSG00000032373	235	common	Car12	carbonic anhydrase 12
In both 1-4 group and 5-8 group	ENSMUSG00000034683	137	common	Ppp1r1c	protein phosphatase 1, regulatory inhibitor subunit 1C
In both 1-4 group and 5-8 group	ENSMUSG00000037034	237	common	Pax1	paired box 1
In both 1-4 group and 5-8 group	ENSMUSG00000050315	356	common	Synpo2	synaptopodin 2
In both 1-4 group and 5-8 group	ENSMUSG00000056174	345	common	Col8a2	collagen, type VIII, alpha 2
In both 1-4 group and 5-8 group	ENSMUSG00000061762	236	common	Tac1	tachykinin 1
In both 1-4 group and 5-8 group	ENSMUSG00000068196	235	common	Col8a1	collagen, type VIII, alpha 1
In both 1-4 group and 5-8 group	ENSMUSG00000073982	245	common	Rhog	ras homolog family member G
In both 1-4 group and 5-8 group	ENSMUSG00000078864	125	common	Gm14322	predicted gene 14322
In both 1-4 group and 5-8 group	ENSMUSG00000085609	134	common	1700016P03Rik	RIKEN cDNA 1700016P03 gene
In both 1-4 group and 5-8 group	ENSMUSG00000087674	123	common	4930447M23Rik	RIKEN cDNA 4930447M23 gene
In both 1-4 group and 5-8 group	ENSMUSG00000108325	246	common	Gm44898	predicted gene 44898
In both 1-4 group and 5-8 group	ENSMUSG00000109122	146	common	A230103L15Rik	RIKEN cDNA A230103L15 gene
In both 1-4 group and 5-8 group	ENSMUSG00000113121	127	common	Gm35161	predicted gene, 35161

1 Nlgn3R451C/(y or R451C)
2 Syngap1+/−
3 POGZQ1038R/+
4 15q11-13dup/+
5 3q29del/+
6 22q11.2del/+
7 Setd1a+/-
8 CaMKIIαK42R/K42R

Supplementary Figure 7

1431 **Supplementary Figure 7**

1432 Pseudocolor presentation of differentially expressed genes (DEGs) between mutant
1433 and corresponding control mice. The number of shared DEGs was higher in the
1434 schizophrenia-related mouse models than in the ASD-related mouse models. Mouse
1435 gene identifiers (ENSMUSG) and gene names for DEGs shared by three or four
1436 schizophrenia-associated mouse models and not differentially expressed in ASD-
1437 associated mouse models are presented. DEGs analyzed for their effects on spines
1438 are shown in red. Color indicates the number of DEGs.

1439 The lower table shows all DEGs shared by three or four mouse models, irrespective of
1440 their grouping as ASD-related or schizophrenia-related.

1441

1442

1443

1444

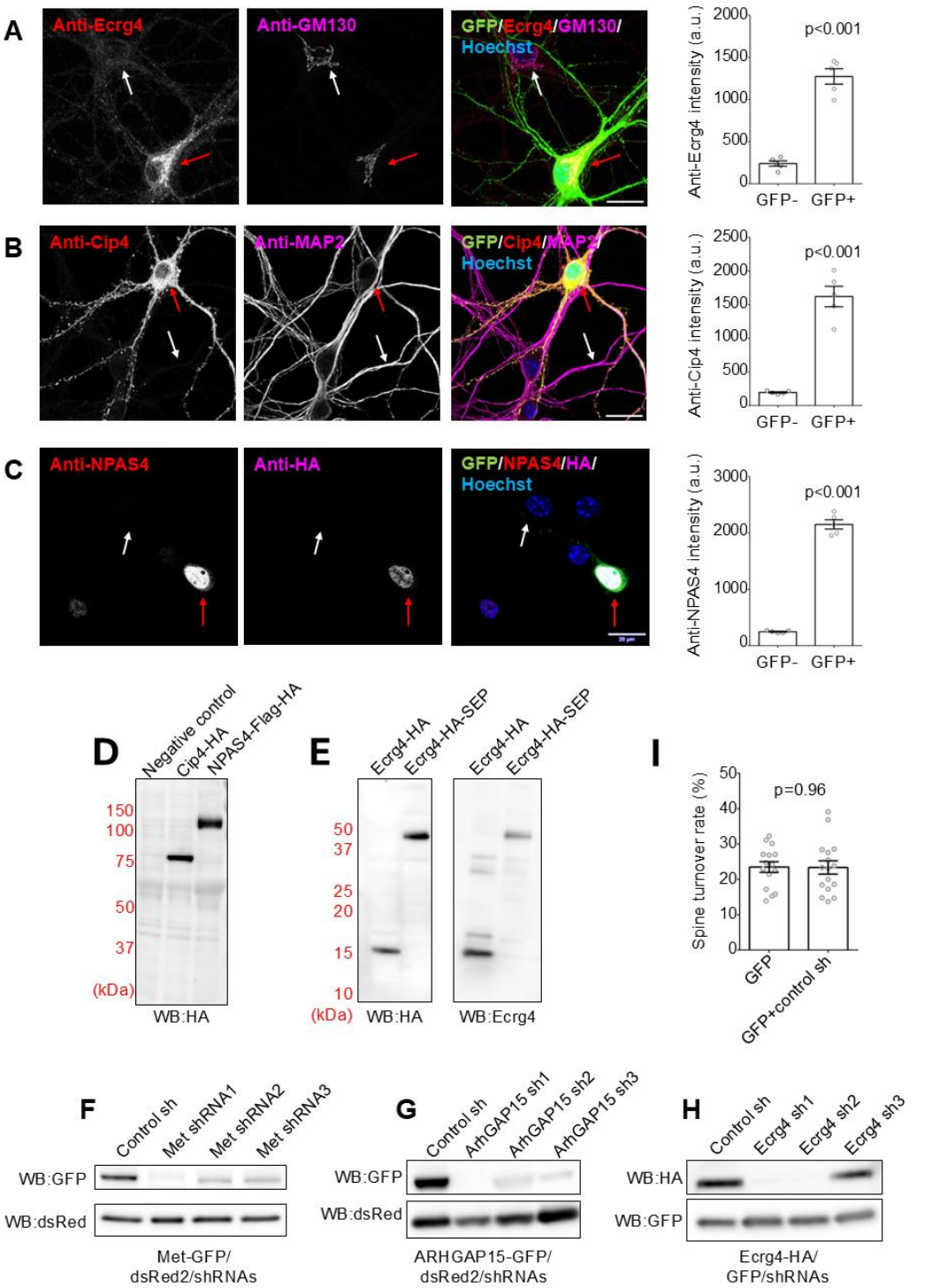

Supplementary Figure 8

1445

1446

1447

1448 **Supplementary Figure 8**

1449 (A-C) Validation of overexpressed tagged constructs by immunocytochemistry in
1450 hippocampal neurons. Bar = 20 μm. The data are presented as mean ± SEM (N = 5
1451 neurons each). Red allows; transfected neurons, white arrows; non-transfected
1452 neurons. (A) Immunocytochemistry of hippocampal neurons expressing Ecrg4-HA with
1453 GFP using anti-Ecrg4 antibody. Anti-GM130 antibody staining detected the Golgi
1454 apparatus. (B) Immunocytochemistry of hippocampal neurons expressing Cip4-HA with
1455 GFP using anti-Cip4 antibody. Anti-MAP2 antibody detected neuronal dendrites. (C)
1456 Anti-NPAS4 and anti-HA immunocytochemistry of hippocampal neurons expressing
1457 NPAS4-Flag-HA with GFP.

1458 (D-E) Immunoblot verification of tagged construct expression in COS-7 cells. (D)
1459 Immunoblotting in total cell lysate from COS-7 cells expressing Cip4-HA or NPAS4-
1460 Flag-HA. The estimated molecular weights of Cip4-HA and NPAS4-Flag-HA are 64
1461 kDa and 89 kDa, respectively. (E) Immunoblotting using both anti-HA and anti-Ecrg4 in
1462 total cell lysate from COS-7 cells expressing Ecrg4-HA or Ecrg4-HA-SEP. The
1463 estimated molecular weights of Ecrg4, Ecrg4-HA, and Ecrg4-HA-SEP are 17 kDa, 18
1464 kDa, and 45 kDa, respectively.

1465 (F-H) Verification of knock-down effects of shRNAs by immunoblotting of COS-7 cells.
1466 Immunoblotting in total cell lysates from COS-7 cells transfected with the expression
1467 vectors of either Met-GFP (F), ArhGAP15-GFP (G), or Ecrg4-HA (H), together with
1468 dsRed2 and shRNAs targeting the corresponding transcripts.

1469 (I) Measurement of spine turnover rate in neurons transfected with a control shRNA
1470 construct together with GFP expression vectors. For the experimental control, we used
1471 neurons transfected only with GFP. The data are presented as mean ± SEM (n = 15

1472 dendrites from 9 neurons for GFP control, n = 16 dendrites from 8 neurons for GFP

1473 plus control shRNA).

1474

1475

1476

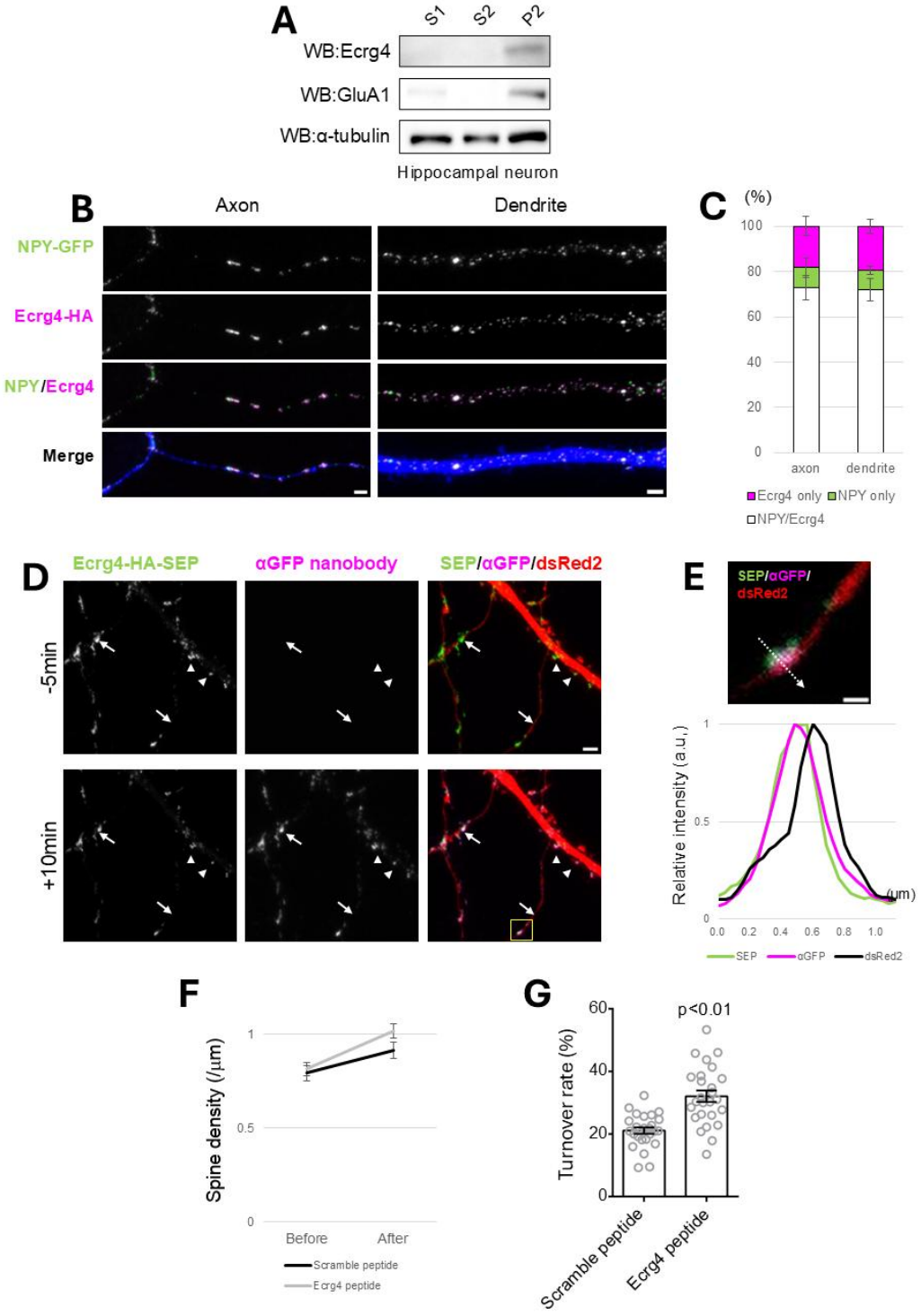

Supplementary Figure 9

1477

1478

1479 **Supplementary Figure 9**

1480 Expression and distribution of Ecrg4 in cultured hippocampal neurons. (A) Preferential
1481 localization of Ecrg4 protein in the membrane fraction. Immunoblotting of Ecrg4,
1482 GluA1AMPA-type glutamate receptor, and α-tubulin in the remaining fraction after
1483 removal of nuclei (S1), supernatant after centrifugation (S2), and resulting pellet (P2).
1484 (B) Images of an immunostained hippocampal neuron expressing HA-tagged Ecrg4
1485 and NPY-GFP. The fluorescence signals were partially colocalized, suggesting Ecrg4
1486 protein accumulation in dense-core vesicles. Bar = 2 μm. (C) Quantification of the
1487 overlap between puncta immunopositive for HA-tagged Ecrg4 and NPY-GFP. N = 4
1488 cells from 1 dish. (D) Surface labeling with the anti-GFP nanobody revealing clusters of
1489 SEP-tagged Ecrg4 in dsRed2-positive axons (arrows) and dendrites (arrowheads). A
1490 nanobody was applied at time t = 0 min. Bar = 2 μm. (E) Enlarged image of a single
1491 Ecrg4 puncta in the axon, marked by a yellow square in (D), with the fluorescence
1492 intensity profile along the dashed arrow. Bar = 0.5 μm. (F) The spine density of cultured
1493 hippocampal neurons 24 hours after administration of either Ecrg4 peptides or
1494 scrambled peptides (n = 26 dendrites and 13 neurons for each condition). (G) Spine
1495 turnover rate of neurons treated with Ecrg4 peptides or scrambled peptides (n = 26
1496 dendrites and 13 neurons for each condition).

1497